ASACUSA STATUS REPORT

ASACUSA progress during 2006 and plans for 2007

ASACUSA collaboration

H.H. Andersen[1], D. Barna[2,7], M. Charlton[3], M. Corradini[4], A. Dax[2], J. Eades[2], Y. Enomoto[5]
R.S. Hayano[2], H. Higaki[6], M. Hori[2], D. Horváth[7], T. Ichioka[8], H. Imao[6], B. Juhász[9], Y. Kanai[6],
H. Knudsen[8], P. Kristiansen[8], N. Kuroda[6], M. Leali[4], E. Lodi-Rizzini[4], C. Malbrunot[9],
B. McCollough[10], S.P. Møller[8], A. Mohri[6], A. Mozzanica[4], Y. Nagata[5], N. Ono[2], T. Pask[9], W. Pirkl[2],
A. Puhm[9], H Saito[11], K. Tokesi[12], H.A. Torii[5], U. Uggerhøj[8], V.L. Varentsov[6], L. Venturelli[4],
E. Widmann[9], Y. Yamazaki[5,6], Z. Yoshida[11], P. Zalan[7], N. Zurlo[4]

*1. Copenhagen University (DK), 2. The University of Tokyo (JP), 3. University of Wales Swansea (GB),
4. Università di Brescia and INFN (IT), 5. The University of Tokyo, Komaba (JP), 6. RIKEN (JP),
7. KFKI (HU), 8. University of Aarhus (DK), 9. Stefan Meyer Institute (AT),
10. The Queen's University of Belfast (GB), 11. The University of Tokyo, Kashiwa (JP), 12. ATOMKI (HU),*

Contents

Executive Summary

In this report we present the main achievements of ASACUSA in 2006 and dicuss preparations for our future progamme of research. The following is a summary of the main points discussed:

Antiprotonic helium spectroscopy

1. We published data from 2004 which showed that $m_{\bar{p}}/m_e = 1836.152674(5)$ (being considered for the CODATA2006 adjustments).

2. Our first sub-Doppler two-photon laser spectroscopy successfully demonstrated that sub-ppb $(< 10^{-9})$ $m_{\bar{p}}/m_e$ measurements will be possible in high-statistics runs in 2007 (6 weeks). If successful, this will complete our programme to measure $m_{\bar{p}}/m_e$ using the $\bar{p}\mathrm{He}^+$-atom laser spectroscopy.

3. We made our first attempts at laser spectroscopy of $\bar{p}\mathrm{He}^{++}$ ions (two-body system). We detected what appears to be a resonance signal, but achieving high precision would require a significant improvement of the methodology. No measurement is planned for 2007.

4. We expect to make an Improved measurement of the hyperfine splitting of antiprotonic helium 4. The CPT limit on the antiproton spin magnetic moment $\mu_{\bar{p}}$, currently 0.3%, will be improved in higher-statistics measurements in 2007 (4 weeks). Hyperfine splitting of antiprotonic helium 3 will be measured in 2008, and further improvement of $\mu_{\bar{p}}$ is planned for 2009.

Atomic/nuclear collisions using slow antiprotons

1. We successfully commissioned a new liquid-helium-free superconducting magnet for antiproton capture/cooling/compression/extraction. About 10^5 antiprotons can now be stably extracted at 250 eV.

2. Using the reaccelerated beam, $\bar{p}$-helium ionization cross sections were measured down to 5 keV. These new measurements seem to have removed the big discrepancies between theory and past experiments (at LEAR), which needs further confirmation in 2007 (2 weeks, plus 2 weeks needed for ultra-slow-beam optimization).

3. Measurements of $\bar{p}$-nucleus annihilation cross sections in gaseous targets at 5 MeV using a fiber scintillator tracker were attempted, but difficulties were found with the AD beam time structure. In 2007, a revised scheme will be tried on solid targets (1.5 weeks).

4. The ultraslow $\bar{p}$ beam and a gas-jet target were used to investigate $\bar{p}$-atom formation cross sections (2 weeks).

Antihydrogen ground-state hyperfine spectroscopy

1. A cryogenic superconducting RF test cavity successfully operated at full power, the design work of the Paul trap for antihydrogen production was completed, and its construction was started.

2. We used an alternative trap design, the so-called cusp trap, to trap electrons. Proton-trapping test is being prepared, and commissioning with antiprotons is planned in 2007 (1.5 weeks).

3. Progress is being made on a positron source based on the buffer-gas cooling method.

Part 1

$\bar{p}$He Spectroscopy

1.1 First sub-Doppler two-photon laser spectroscopy of antiprotonic helium atoms

Introduction

During the beamtime of 2006, the ASACUSA collaboration successfully carried out the first sub-Doppler laser spectroscopy experiments of antiprotonic helium [1] atoms. This constitutes the first time an antiproton has been excited between atomic states by a non-linear multiphoton process, all such experiments having previously been done for electrons. This success opens the way in 2007 to the carrying out of CPT symmetry tests at even higher precisions (< 1 ppb) than in our past experiments. In 2006 we also published our 2004 measurements which yielded a new value for the antiproton-to-electron mass ratio in good agreement with the corresponding proton-to-electron value [2].

Antiproton-to-electron mass ratio

In the abovementioned publication,12 transition frequencies of antiprotonic helium atoms were measured to the then highest precisions of $(9-16) \times 10^{-9}$ [2]. Comparison of these results with the latest three-body QED calculation by Korobov [3–5] which had a precision of $(1-2) \times 10^{-9}$ then yielded an antiproton-to-
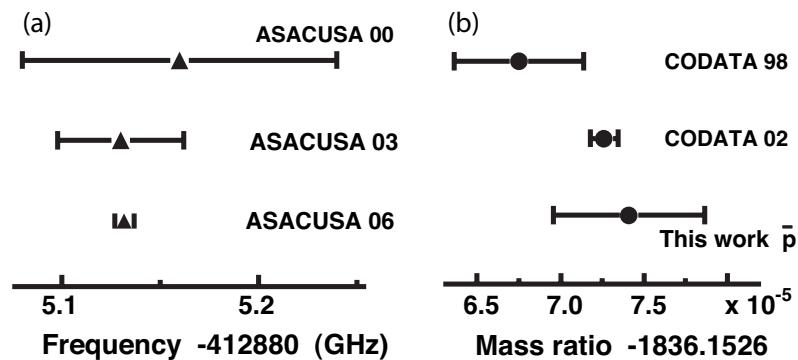
Figure 1.1: *(a): Frequency of the $\bar{p}^4$He$^+$ transition $(n, \ell) = (37, 35) \rightarrow (38, 34)$ measured by the ASACUSA collaboration over the years. (b): Proton-to-electron mass ratios recommended by the CODATA 98 and 2002 compilations, and the antiproton-to-electron mass ratio determined by ASACUSA.*

electron mass ratio,

$$\frac{M_{\bar{p}}}{m_e} = 1836.152674(5). \tag{1.1}$$

The error 5 on the last digit above is the quadratic sum of 4 (the statistical experimental error), 3 (arising from the experimental systematic error), and 2 (from the precision of the theoretical calculation). The above value of $\frac{M_{\bar{p}}}{m_e}$ was in good agreement with the known proton-to-electron mass ratio recommended by the CODATA 98 and 2002 compilations [6],

$$\frac{M_p}{m_e} = 1836.1526675(39), \tag{1.2}$$

$$\frac{M_p}{m_e} = 1836.15267261(85). \tag{1.3}$$

It should be noted that the result 1.1 is derived from our data alone, and requires no supplementary measurement of another measured variable. We were also able to set a new limit on the possible difference between the antiprotonic charge ($Q_{\bar{p}}$) and mass ($M_{\bar{p}}$), and the values for the proton (Q_p and M_p) [7]. In this case, our measured $\bar{p}\mathrm{He}^+$ transition frequencies, which scale with the antiproton Rydberg constant ($R_{\bar{p}} \propto M_{\bar{p}} Q_{\bar{p}}^2$) had (as in all our previous determinations) to be supplemented by the cyclotron frequency ($\omega_{\bar{p}} \propto Q_{\bar{p}} B / M_{\bar{p}}$), the observable measured in Penning trap experiments, Here, the TRAP collaboration has experimentally set an upper bound on any difference between the antiproton and proton cyclotron frequencies to be $\frac{q}{m}(\bar{p})/\frac{q}{m}(p) + 1 = 1.6(9) \times 10^{-10}$ [8, 9]. Limits on the charge and mass were deduced from the equation [1, 7],

$$\delta = \frac{Q_p + Q_{\bar{p}}}{Q_p} \sim \frac{M_p - M_{\bar{p}}}{M_p} = \frac{1}{f} \frac{v_{th} - v_{exp}}{v_{exp}}. \tag{1.4}$$

Values of 2.5–6.1 for f were estimated by noting that when Kino *et al.* [5] changed the values of the antiprotonic charge and mass by 1 ppm (under the stringent constraint of Ref. [8] on any CPT violation on $\omega_{\bar{p}}$), the transition energies changed by 2.5–6.1 ppm depending on the transition. A value of $\delta = (-3 \pm 14) \times 10^{-10}$ was obtained, which implies that the antiproton charge and mass agree with the proton's to a precision of 2×10^{-9} at a confidence level of 90%. The error 14 on the last two digits above is the quadratic sum of 11 (the statistical experimental error), 8 (arising from the experimental systematic error), and 5 (from the precision of the theoretical calculation).

Sub-Doppler two-photon laser spectroscopy

In Fig. 1.2, limits $\delta_{\bar{p}}$ on the possible differences between the antiproton charge and mass $Q_{\bar{p}}$ and $M_{\bar{p}}$, and the corresponding proton values (M_p and Q_p) derived from measurements of $\bar{p}\mathrm{He}^+$ made by ASACUSA over the years are shown. The 2004 experiment described above was carried out using an optical comb generator [10, 11] in conjunction with a continuous-wave pulse-amplified dye laser.

Now the precision of this 2004 experiment was limited by the Doppler broadening of the atomic lines of $\bar{p}\mathrm{He}^+$, which arises from the thermal motion of the atoms in the helium gas target cooled to temperature $T = 5\text{-}10$ K where the atoms were formed. The Doppler effect caused the measured lines to take on a Gaussian shape with a full-width-at-half-maximum of

$$\Delta v = 2.35 \frac{v}{c} \sqrt{\frac{kT}{M}}, \tag{1.5}$$

wherein v denotes the resonance frequency, k the Boltzmann constant, and M the mass of the $\bar{p}\mathrm{He}^+$ atom. For example, the resonance profile of the transition $(n, \ell) = (36, 34) \rightarrow (35, 33)$ at wavelength $\lambda = 417$ nm shown in Fig. 1.3 (top) has a width ~ 1 GHz, which was mostly due to the Doppler broadening and the hyperfine structure arising from the interaction between the antiproton orbital angular momentum and electron
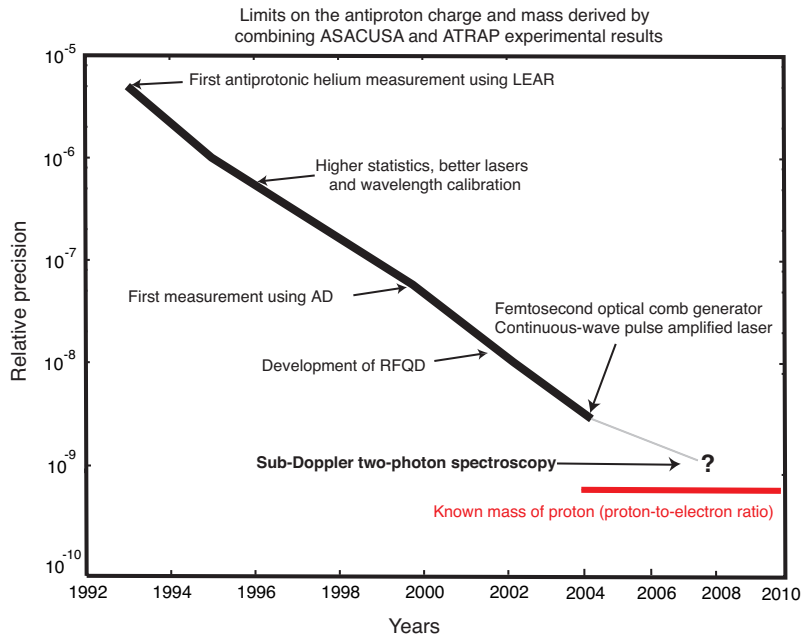
Figure 1.2: *Limit δ_{CPT} on the possible differences between the antiproton mass $M_{\bar{p}}$ and charge $Q_{\bar{p}}$, and those of the proton's measured over the years, derived by combining the results of the $\bar{p}\text{He}^+$ laser spectroscopy and Penning trap experiments carried out by the TRAP collaboration. The experimental techniques used to improve the precision on the $\bar{p}\text{He}^+$ transition frequencies over the years are indicated.*

spin. In fact, the profile is theoretically expected to be a superposition of four partially overlapping peaks, the calculated positions of which are indicted by red arrows in Fig. 1.3. Of course, individual hyperfine peaks cannot be resolved here due to the much larger Doppler broadening. No further improvement in the experimental precision of the transition frequency was possible unless this broadening could be reduced or eliminated. Our 2006 experiments succeeded in doing this using a new technique.

Generally, laser spectroscopic measurements of normal atoms and molecules at the highest precision utilize two laser beams arranged in a counterpropagating geometry, that effectively eliminates this Doppler broadening to first order. For example, the frequency of the 1s-2s two-photon transition in atomic hydrogen has been measured to precisions of $\sim 10^{-14}$, by irradiating the atoms with two counterpropagating laser beams of the same wavelength $\lambda = 243$ nm equal to half the 1s-2s interval. It is not possible, however, to directly apply this Doppler-canceling technique to our $\bar{p}\text{He}^+$ experiments, because the transition probabilities involved in any non-linear two-photon transition of the antiproton are many orders of magnitude smaller than e.g., the electron case in hydrogen. Indeed, calculations reveal that the laser intensities that would be needed to excite such a $\bar{p}\text{He}^+$ transition within the microsecond-scale lifetime of the atom, using two photons of equal wavelength are much greater than those available from any tunable laser.

We here solved these problems by utilizing a near-resonant two-photon excitation (Fig. 1.4). The two counter-propagating laser beams irradiating the $\bar{p}\text{He}^+$ had non-equal frequencies ν_1 and ν_2, which were adjusted such that i): their combined frequencies $\nu_1 + \nu_2$ were tuned to the two-photon transition $(n, \ell) = (36, 34) \rightarrow (34, 32)$ involving an angular momentum change of $\Delta\ell = 2$, ii): the virtual intermediate state involved in the two-photon transition was tuned to within a few GHz of a real state $(n, \ell) = (35, 33)$. The nearness of the virtual state to a real one led to an enhancement of the two-photon transition probability by several orders of magnitude compared to the case $\nu_1 = \nu_2$. Under these conditions, the observed width $\Delta\nu_{2\gamma}$ of the resonance line decreased by factor 20 compared to the thermal Doppler width $\Delta\nu$ according to the
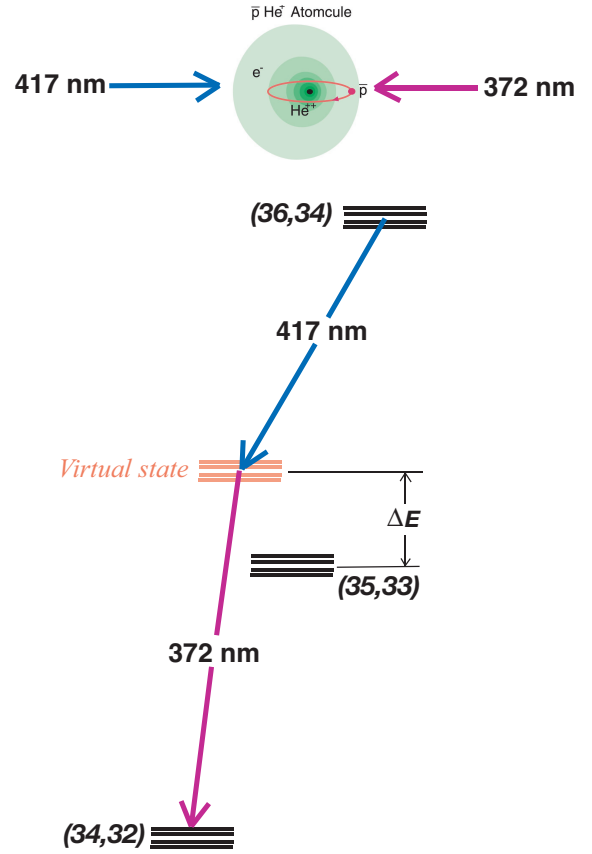
2004: Single-photon spectroscopy
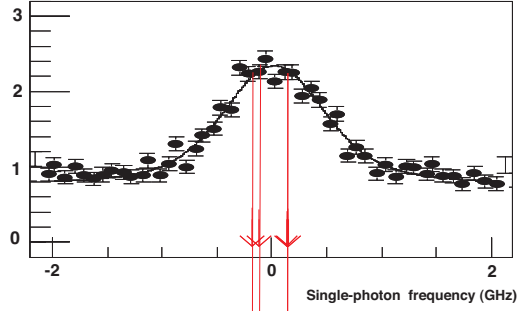
2006: Two-photon spectroscopy
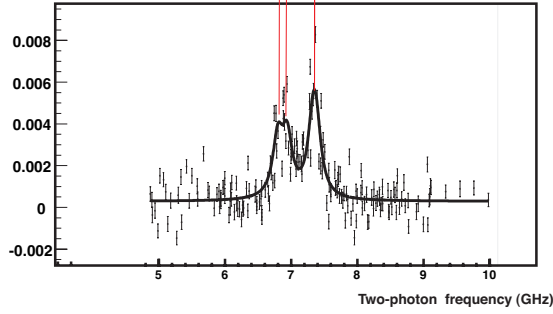
Figure 1.3: *Resonance profile of the Doppler-broadened single-photon transition $(n,\ell) = (36,34)\rightarrow(35,33)$ of $\bar{p}^4\mathrm{He}^+$ measured in 2004 (top). Red arrows denote the theoretical positions of the hyperfine components. Sub-Doppler resonance profile of the two-photon transition $(n,\ell) = (36,34)\rightarrow(34,32)$ measured in 2006 using two counterpropagating laser beams (bottom). The spectral resolution was increased by an order of magnitude.*

Figure 1.4: *Energy level diagram of antiprotonic helium, indicating the principle of sub-Doppler two-photon spectroscopy.*

equation,

$$\Delta\nu_{2\gamma} = \left|\frac{\nu_1 - \nu_2}{\nu_1 + \nu_2}\right|\Delta\nu. \tag{1.6}$$

This measurement required two UV lasers with intensities and resolutions that were much higher than those used in our 2004 experiments.

New experimental setup

A new experimental setup (Fig. 1.5) was developed to carry out these two-photon experiments in 2006. Antiprotons extracted from the AD were decelerated to energy 80 keV using the radiofrequency quadrupole decelerator (RFQD), and entered a cryogenic helium gas target through a 1-micron-thick PEN plastic window [12]. The target was filled with helium gas of pressure $P \sim 1$ mb and temperature $T = 6$ K. The $\bar{p}\mathrm{He}^+$ atoms produced in this way were irradiated by two counterpropagating laser beams of wavelength $\lambda = 372$ nm and 417 nm, energy $P = 15$ mJ, pulse-length $\Delta t = 30$ ns, and diameter $d = 20$ mm. The laser beams entered the target through two fused silica windows of diameter $d = 120$ mm and thickness $t = 10$ mm, mounted perpendicular to the antiproton beam. The windows were adjusted at Brewster's angle which minimized any reflection of the linearly-polarized laser beams off their surfaces. The laser beams
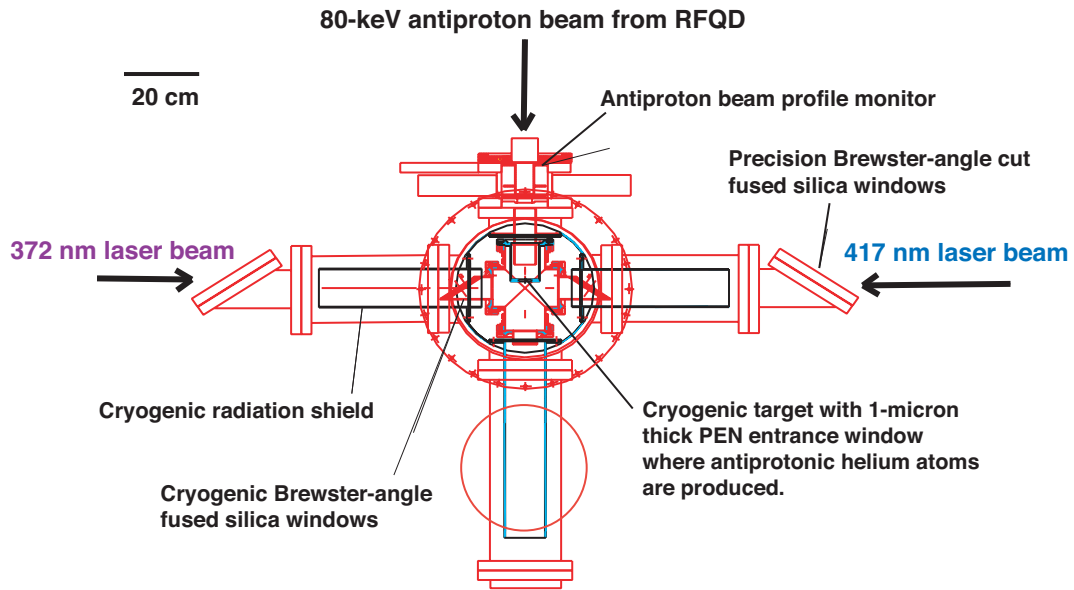
Figure 1.5: *New experimental setup installed in 2006 to carry out sub-Doppler two-photon laser spectroscopy of antiprotonic helium.*
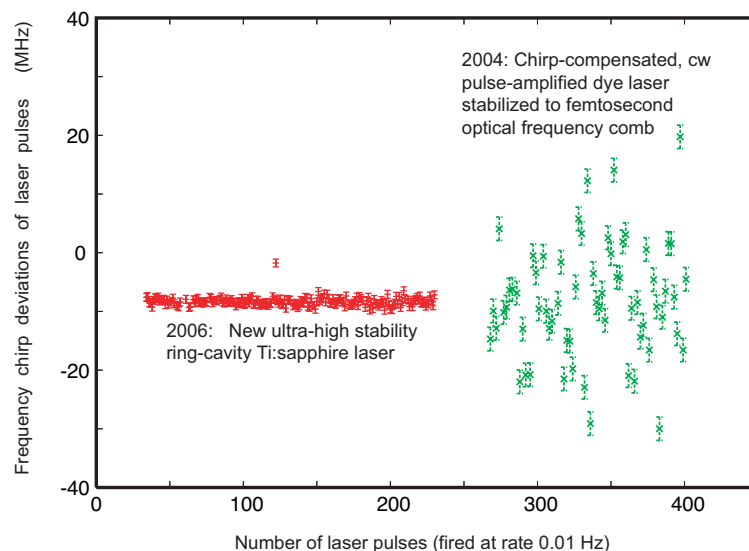
Figure 1.6: *Comparisons of the shot-to-shot frequency stability of (left) new ultra-high stability ring-cavity Ti:sapphire laser developed by ASACUSA, and used for the first time in the 2006 experiments, and (right) those of the previous chirp-compensated, cw pulse-amplified dye laser stabilized to a femtosecond frequency comb used in our 2004 experiments.*

induced the non-linear two-photon transition $(n,\ell) = (36,34) \rightarrow (34,32)$, which resulted in the immediate Auger emission of the electron, followed by antiproton annihilation in the helium nucleus. Charged pions emerging from the annihilation were detected by Cherenkov counters made of UV-transparent Lucite which surrounded the target. This signaled the resonance condition between the two laser beams and the atom.

To carry out these measurements with the highest precision, we developed two sets of pulsed Ti:sapphire

lasers whose optical frequencies were stabilized with a precision of $\sim 10^{-10}$ against an optical frequency comb. Each laser produced 30-ns-long laser pulses of energy 40 mJ and wavelength $\lambda = 745$–834 nm, which were frequency-doubled using non-linear crystals to generate UV beams of $\lambda = 372$–417 nm. Our frequency stability and resolution now rivals those of the most precise nanosecond pulsed lasers reported in literature, which were used in e.g., the 1s-2s two photon spectroscopy measurements of hydrogen or muonium [13]. In Fig. 1.6, the fluctuations in the optical frequency of individual laser pulses (the so-called "frequency chirp") emitted from the new Ti:sapphire laser (left) are compared with those of the previous pulsed dye laser used in our 2004 experiments (right). As a result of numerous technical developments, the new laser has a frequency stability (~ 1 MHz) which is factor > 10 better than before.

Experimental results

In Fig. 1.3 (bottom), the resonance profile of the two-photon transition $(n, \ell) = (36, 34) \rightarrow (34, 32)$ measured in this way is shown. The spectral resolution (~ 170 MHz) is now sub-Doppler and an order of magnitude higher compared to the previous Doppler-broadened case [Fig. 1.3 (top)]. The hyperfine lines spaced at intervals ~ 500 MHz can be clearly resolved. We measured these resonance lines at various detunings ± 4–12 GHz of the virtual intermediate state from the real state $(n, \ell) = (35, 33)$. This data is now being analyzed. Preliminary results indicate that this sub-Doppler method may yield an improvement in the experimental precision of the $\overline{p}\mathrm{He}^+$ atomic transition frequencies to several parts per billion (i.e., $m_{\overline{p}}/m_e$ measured to ~ 0.5 ppb, as precise as the CODATA 2002 m_p/m_e precision), provided that more detailed systematic studies are carried out in 2007.

1.2 First attempts at laser spectroscopy of the two-body antiprotonic helium ion

Introduction

In 2003, we produced and systematically studied for the first time large numbers ($N \sim 10^9$) of cold (temperature $T \sim 10$ K), long-lived antiprotonic helium $\overline{p}\mathrm{He}^{2+}$ ions [14]. In 2006, we attempted the first laser spectroscopy measurements of $\overline{p}\mathrm{He}^{2+}$. These ions constitute ideal semiclassical Bohr systems whose spin-independent parts of the energy levels (left side of Fig. 1.7) can be theoretically calculated to very high precision ($\sim 10^{-8}$) using the simple equation,

$$E_n = -\frac{4R_\infty hc}{n_i^2} \frac{M}{m_e} \frac{Q_{\overline{p}}^2}{e^2} \tag{1.7}$$

where the reduced mass of the system is denoted by M, the electron mass by m_e, the Rydberg constant by R_∞, and the antiproton and electron charges by $Q_{\overline{p}}$ and e. This ion may be a better candidate than the more complicated three-body $\overline{p}\mathrm{He}^+$ atom for determining the properties of antiprotons at the highest precision, due to the extreme ease in calculating its energy levels. We therefore attempted to measure the ionic transition $(n, \ell) = (29, 28) \rightarrow (30, 29)$ at the deep UV wavelength 212.3 nm.

Experimental realization and results

Three-body $\overline{p}{}^3\mathrm{He}^+$ atoms were first produced using the experimental setup of Fig. 1.5. A laser pulse of short duration $\Delta t < 700$ ps, wavelength $\lambda = 463$ nm, and energy $E = 3$ mJ was fired into the target, thereby inducing the transition $(n, \ell) = (36, 34) \rightarrow (35, 33)$ which resulted in Auger emission and the production of $\overline{p}{}^3\mathrm{He}^{2+}$ ions occupying state $(30, 29)$ (see Fig. 1.7). This laser pulse was produced by allowing 3-ns-long
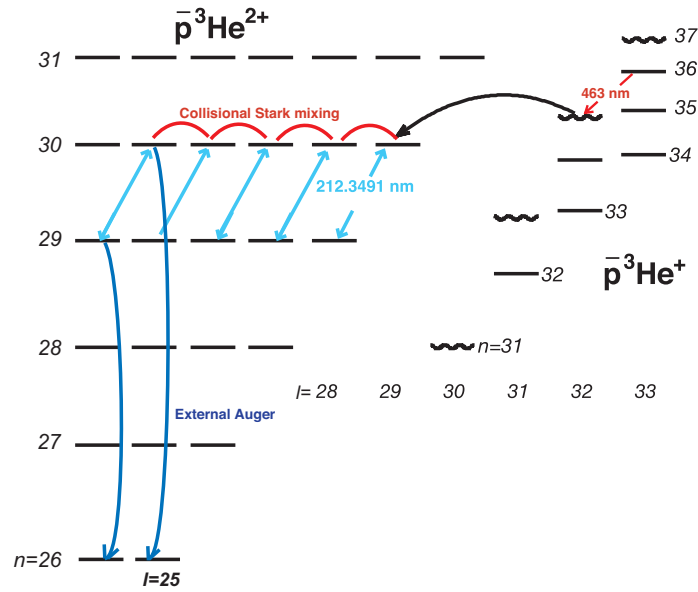
Figure 1.7: *Portions of the energy level diagrams of $\bar{p}\mathrm{He}^+$ atoms and $\bar{p}\mathrm{He}^{2+}$ ions. The cascade processes of the atoms and ions are indicated with arrows.*

laser pulses of wavelength $\lambda = 532$ nm from a Nd:YAG laser to pass through a 1-m-long stimulated Brillouin scattering (SBS) cell. The non-linear SBS process compressed the laser pulses to duration $\Delta t < 700$ ps, and these were then used to pump an organic dye laser. Immediately afterwards, a second laser pulse of wavelength $\lambda = 212.3$ nm, energy $E = 8$ mJ, and pulse-length $\Delta t = 15$ ns induced transitions between ionic states with n-values of 29 and 30. This second laser beam was generated using the pulsed ring Ti:sapphire laser described above. The output of $E = 30$ mJ and $\lambda = 849.2$ nm was frequency-quadrupled using two beta barium borate (BBO) crystals.

In Fig. 1.8, part of the delayed annihilation time spectrum (the distribution of the number of antiproton annihilations, as a function of time elapsed since the neutral $\bar{p}^3\mathrm{He}^+$ atom was formed), measured by simultaneously irradiating the target with the 463-nm and 212-nm lasers are shown. Normalized spectra measured at 9 wavelength settings of the 212-nm laser are shown superimposed, and the fundamental wavelength which was frequency-quadrupled to produce the 212-nm laser beam are indicated for each spectrum. Each spectrum is the addition of data recorded from 50 antiproton pulses which took 1.5 h to measure. We found that when the 212-nm laser was tuned exactly on the theoretical resonance wavelength of the ion $\lambda = 212.3491$ nm, the position of the peak (i.e., its weighted mean) appears to shift by a very small amount (0.5 ns) to earlier times. This effect, if it is true, may indicate that the on-resonance laser which deexcites the ions to states $n = 29$ may be causing a slight shortening in the overall cascade lifetime of the ion.

In Fig. 1.9, the weighted average position of the annihilation spike at various wavelength settings of the 212-nm laser are shown. The red arrow shows the position of the theoretically-expected $\bar{p}^3\mathrm{He}^{2+}$ resonance wavelength. This spectrum is a summation of data taken over several days, each data point containing a few hundred antiproton pulses. As can be seen, there may be a small peak at exactly the expected position, but these first measurements showed that various improvements must be made to the experimental setup in order to achieve higher S/N ratios.
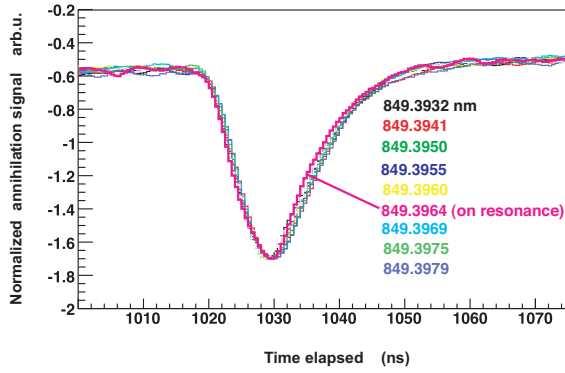
Figure 1.8: *Delayed annihilation time spectra measured by irradiating the $\overline{p}^3\text{He}^+$ with a 463-nm laser pulse (thus producing a $\overline{p}^3\text{He}^{2+}$ ions), followed by a second laser tuned on and off the ionic resonance between $n = 29$ and 30. Normalized spectra measured at 9 wavelength settings of the 212-nm laser are shown superimposed. The fundamental wavelengths which were frequency-quadrupled to produce the 212-nm laser beam are indicated.*
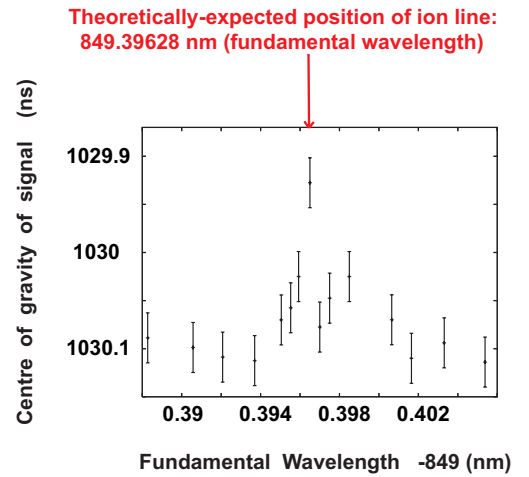
Figure 1.9: *Weighted average position of the annihilation spike at various wavelength settings of the 212-nm laser around the theoretically-expected value of the $\overline{p}^3\text{He}^{2+}$ resonance. The fundamental wavelength which was frequency-quadrupled to produce the 212-nm laser beam is indicated.*

1.3   Improved measurement of the hyperfine splitting of $\overline{p}^4\text{He}^+$

Introduction

It has been shown during the 2006 beam time that an improved determination of the hyperfine (HF) splitting of $\overline{p}\text{He}^+$ is possible. Through the utilization of a pulse-amplified cw laser system developed by ASACUSA in 2004 [15], the precision relative to the 2001 measurement [16] has been increased by a factor 5, according to preliminary data analysis. With more statistics and a density dependent study, this factor of accuracy can be increased to 10, yielding an improved value for the spin magnetic moment of the antiproton (by a factor 3) and a new test of QED theory and CPT.

The goal for 2007 is to measure the $(n, L) = (37, 35)$ transition energy of $\overline{p}^4\text{He}^+$ to the highest possible degree of meaningful precision. A recent analysis [17] of the sensitivity of 3-body QED calculations to the spin-magnetic moment $\vec{\mu}_{\overline{p}}$ of the antiproton has produced clear predictions of the maximum obtainable improvement of $\vec{\mu}_{\overline{p}}$ for each (n, L)-state of $\overline{p}^4\text{He}^+$. After this step has been completed other hyperfine states are of interest. The entire program is expected to take 2-3 years, during which time the first measurements on $\overline{p}^3\text{He}^+$ are intended, where agreement between theory and experiment is not so clear in the case of laser transitions [15], and a second $\overline{p}^4\text{He}^+$ state, for an even better test of CPT invariance.

CPT Invariance

The implication of CPT invariance is that all the properties of particles and their antiparticles must be identical. Over the past five years the ASACUSA collaboration has measured the transition frequencies of antiprotonic helium with an ever increasing degree of accuracy [15]. Comparison with QED calculations have determined the antiproton-to-electron mass ratio to high precision. The antiproton spin magnetic moment is known to a far lesser degree. The most accurate measurement to date was made in 1988 [18].

The hyperfine structure of antiprotonic helium comes about via the interaction of the antiproton spin with
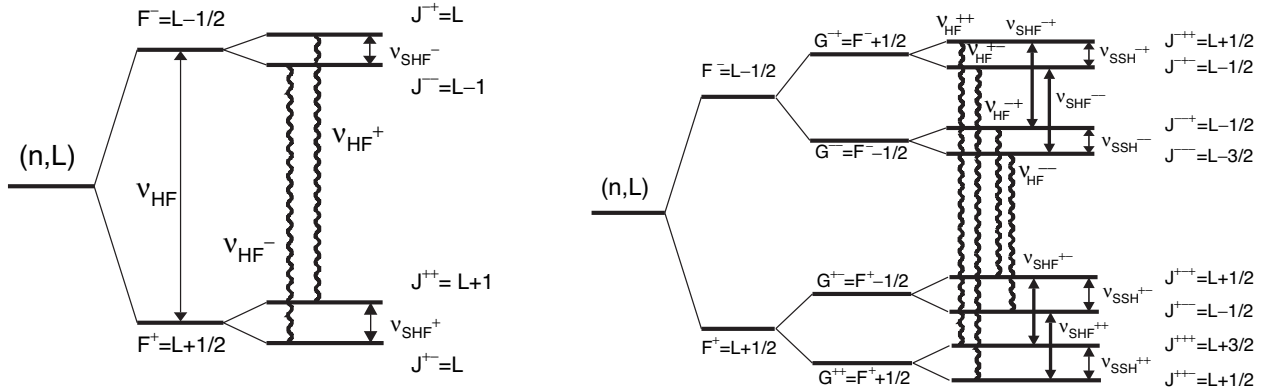
Figure 1.10: *Hyperfine structure of $\overline{p}^4He^+$ (left) and $\overline{p}^3He^+$ (right). Wavy lines denote M1 transitions that correspond to a spin flip of the electron (HF transitions) which can be detected with our laser-microwavelaser method described later, while double arrows symbolize M1 transitions with spin flips of the antiproton or the helion.*

its angular momentum and the electron spin. An experimental measurement of the hyperfine structure can be compared with QED calculations [19] to determine the difference between the antiproton and proton spin magnetic moment. Indeed this was already determined in our 2001 measurement to an accuracy within 1.6% [16]. The current PDG value is 0.3 % [20]. During the 2006 beam time a systematic study was commenced that, coupled with further studies in 2007, will see the precision of the anti-protonic spin magnetic moment measured to 0.1%.

The Hyperfine Structure of Antiprotic Helium

The HFS of $\overline{p}He^+$ arises from the interaction of the magnetic moments of its constituents. Due to the large orbital angular moment of the antiproton ($L_{\overline{p}} \sim 35$), the dominant splitting arises from the interaction of $\overrightarrow{L}_{\overline{p}}$ with the electron spin $\overrightarrow{S}_e$. The antiproton spin $\overrightarrow{S}_{\overline{p}}$ and the spin $\overrightarrow{S}_h$ of the 'helion' h, the ^{3}He nucleus, lead to further splittings leading to a quadruplet for $\overline{p}^4He^+$ and an octet for $\overline{p}^3He^+$ (Fig. 1.10).

The hierarchy of angular moments and the angular momentum coupling schemes are shown in tables 1.1 and 1.2(numerical values from CODATA2002; $\mu_{\overline{p}} = -2.800(8)\mu_N$ (PDG)):

$\overrightarrow{\mu}_e = g_e\mu_B\overrightarrow{S}_e$	= -1.001 159 652 1859(38)μ_B
$\overrightarrow{\mu}_{\overline{p}}^\ell = g_\ell^{\overline{p}}\mu_N\overrightarrow{L}_{\overline{p}}$	$\sim$ 1.906 159 $\times 10^{-2}\mu_B$
$\overrightarrow{\mu}_{\overline{p}}^s = g_s^{\overline{p}}\mu_N\overrightarrow{S}_{\overline{p}}$= 2.792 847 351(28) $\mu_N(p)$= 1.521 032 206(15) $\times 10^{-3}\mu_B$
$\overrightarrow{\mu}_h = g_h\mu_N\overrightarrow{S}_h$ = -2.127 497 723(25) μ_N	= -1.158 671 474(14)$\times 10^{-3}\mu_B$

Table 1.1: *Hierarchy of angular momentums*

Although the helion magnetic moment is smaller than that of the antiproton, its overlap with the electron cloud (which is in the ground state and has its maximum probability at the helion site) is stronger and therefore the above coupling scheme is more stable.

In Fig. 1.10 allowed M1 transitions that can be induced by an oscillating magnetic field are shown. In the case of $\overline{p}^4He^+$, there are two types of transitions: hyperfine (HF) transitions (ν_{HF}^+ and ν_{HF}^-) which are associated with a spin-flip of the electron, and superhyperfine (SHF) transitions (ν_{SHF}^+ and ν_{SHF}^-) which are associated with a spin flip of the antiproton.

$\bar{p}^4He^+$	$\bar{p}^3He^+$
$\vec{F} = \vec{L}_{\bar{p}} + \vec{S}_e$	$\vec{F} = \vec{L}_{\bar{p}} + \vec{S}_e$
$\vec{J} = \vec{F} + \vec{S}_{\bar{p}} = \vec{L}_{\bar{p}} + \vec{S}_e + \vec{S}_{\bar{p}}$	$\vec{G} = \vec{F} + \vec{S}_h = \vec{L}_{\bar{p}} + \vec{S}_e + \vec{S}_h$
	$\vec{J} = \vec{G} + \vec{S}_{\bar{p}} = \vec{L}_{\bar{p}} + \vec{S}_e + \vec{S}_h + \vec{S}_{\bar{p}}$

Table 1.2: *Angular momentum couplings*

Laser Microwave Spectroscopy

It is only possible to induce a transition between super hyperfine states with microwave (M1) transitions. Initially all the SHF states are equally populated and so a population asymmetry must first be induced to study the transfer between them. A laser transition (E1) between one of the hyperfine doublets (n, L, F) and a corresponding doublet (n', L', F') of a short lived daughter state creates this asymmetry. A microwave pulse then follows, inverting the asymmetry. A second, laser pulse, of the same wavelength as the first, is used to depopulate the state again, after it has been partially refilled by resonant microwave-stimulated transitions. Since the short lived daughter state has a lifetime three orders of magnitude shorter than the parent, a sharp annihilation peak, corresponding to the induced depopulation, can be detected using Cherenkov counters. If the microwave frequency is varied the second annihilation peak will be larger on resonance than off. Hence the process is called a laser-microwave-laser method.

Results From 2006

The state chosen for study is $(n, L) = (37, 35)$. There are two E1 (726 nm wavelength) laser transitions (f^+ and f^-) between the $(n, L) = (37, 35)$ and $(38, 34)$ states corresponding to transitions between the HF doublets (F^+ and F^-). The four transitions shown as four in Fig. 1.11 can only be resolved in our experiments into two resonant peaks on account of Doppler broadening. A comparison between the laser resonance profile obtained with the old pulsed dye laser in 2001 and a similar scan from 2006 is shown in Fig. 1.12. In both graphs the two resonance peaks at wavelengths λ_+ and λ_- differ by 1.8 GHz but they are resolved much more clearly in the second scan. The new laser system is evidently more stable, verified by the points which, in the first graph, fluctuate much more than the second.

Scans such as the second graph in Fig. 1.12 were taken at three different densities (150, 250, 500 mbar) and at various laser powers as part of a systematic study. Due to time constraints microwave studies were conducted at only one helium density (250 mbar).

The laser pulse separation in the 2001 experiment (which determines the microwave pulse length) was limited to 150 ns. Our recent improvements in the laser system have now removed this limit. A 'microwave on-off' test was conducted. The laser was tuned to the f^+ transition and pulsed twice at various time intervals. The microwave was tuned to the ν_{HF}^+ resonance. A Comparison of the second laser induced annihilation peaks, between when the microwave was on and off, shows the time dependant signal to noise ratio. Such a scan is presented in Fig. 1.13 where the signal to noise is increased by a factor of 4-5 for the same laser separation used in 2001. These results, in conjunction with other laser measurements, reveal information about the frequency of the population-relaxing spin-flip collisions. They provide important input for theoretical calculations [21] and will, after further analysis, be publishable.

For laser-microwave-laser scans the laser wavelength was tuned to the transition f^+: between the F^+ doublets of $(n, L) = (37, 35)$ and the short lived daughter state $(n, L) = (38, 34)$. Under the incident laser light F^+ undergoes a significant depopulation while the population of F^- is only slightly reduced due to its different transition frequency. The daughter state decays through Auger transitions and then annihilates in a matter of ~ 10 ns, so that the depopulation of the sate can be measured with Cherenkov counters. This
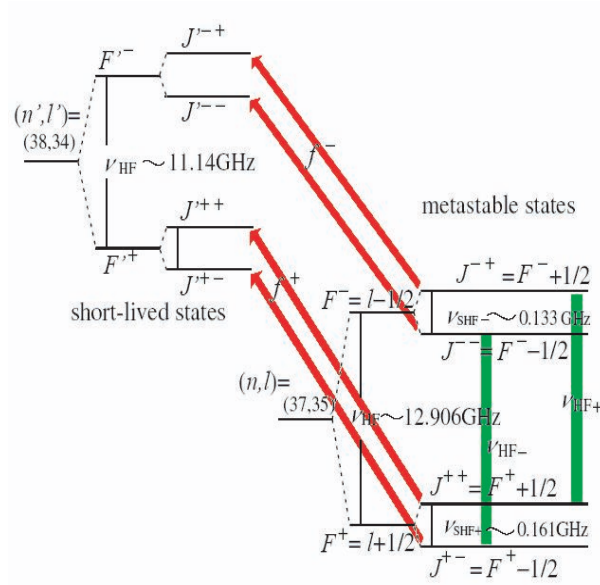
Figure 1.11: *Energy level diagram showing the various hyperfine and super hyperfine structures of the parent state $(n,L) = (37,35)$ and the daughter state $(38,34)$. The laser transitions, from the parent to daughter state, are indicated in red and the microwave transitions, within the parent state, in green.*
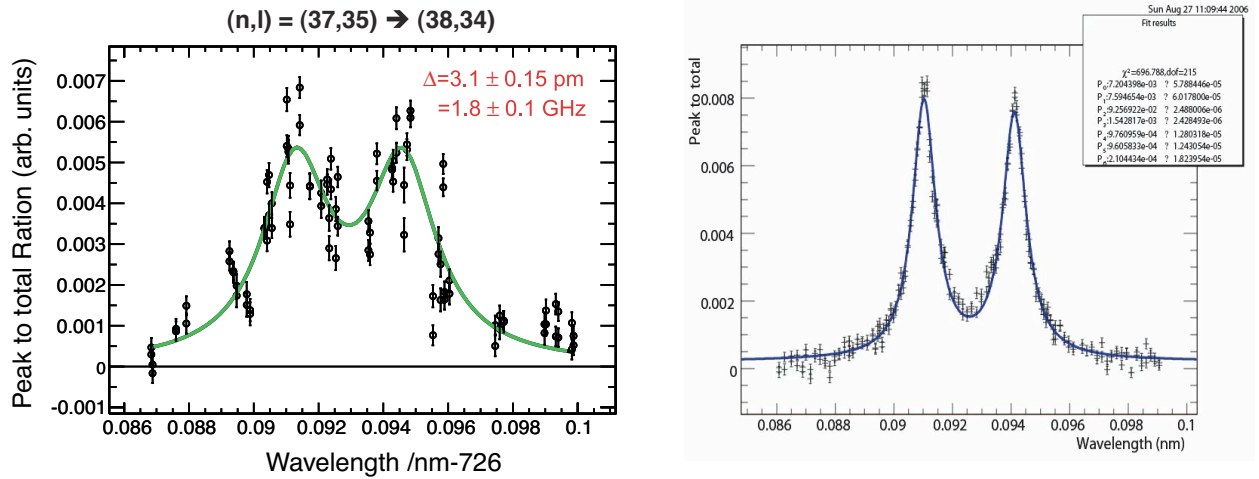
Figure 1.12: *Laser resonance profile of the $(n,L) = (37,35)$ to $(38,34)$ transition measured at the AD ring in 2001 (left) and 2006 (right). The resonance centre wavelengths λ_+ and λ_- are evident. in 2001 the two HF transitions cannot be clearly separated due to the large band width of the pulsed laser. In 2006 the reduced band width allows the transitions to be well resolved, resulting to an increase of the achievable population asymmetry between the F^+ and F^- HF doublets.*
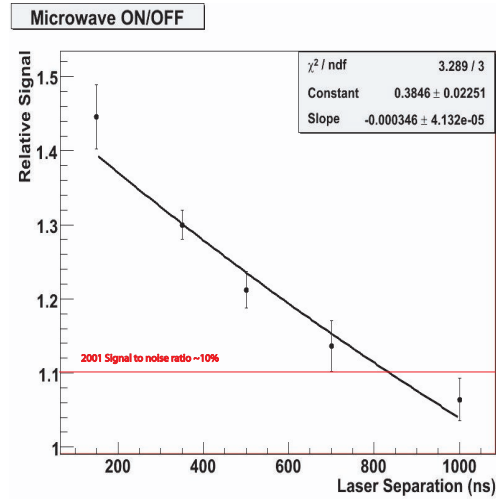
Figure 1.13: *Microwave on-off measurement showing the reduction in signal as the laser separation is increased.*
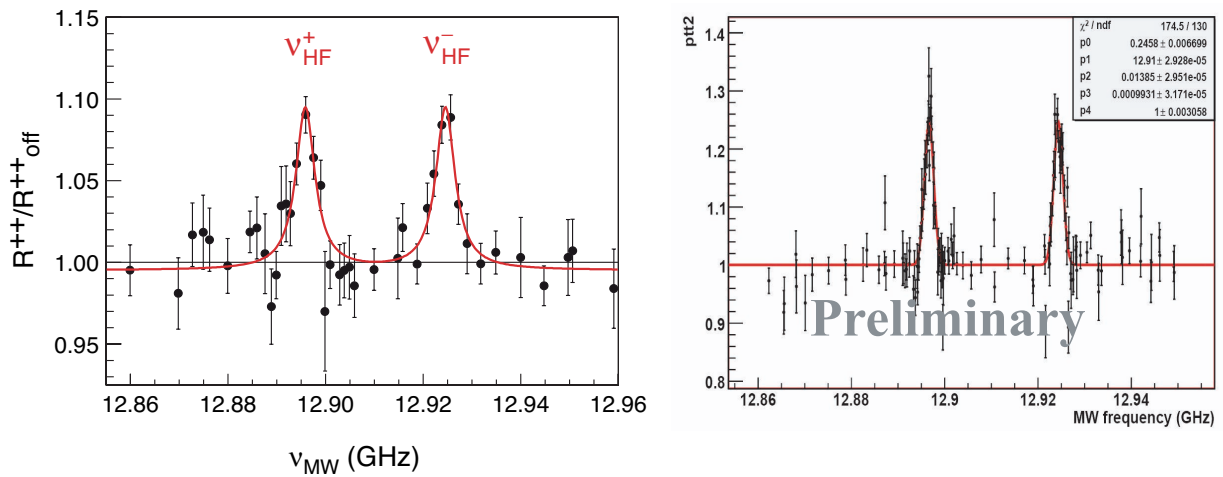
Figure 1.14: *Microwave resonance profile of the (37, 35) metastable state showing the ν_{HF}^+ and ν_{HF}^- peaks. The data was taken at the AD ring in CERN in 2001 (left) and 2006 (right).*

process causes a population asymmetry between the two hyperfine states. A microwave pulse of ~ 4 Gauss is then used to create a population transfer such that F^+ is refilled from F^- and thus has a replenished population when the second laser pulse arrives. The final stage of the experiment occurs when the delayed laser depopulates F^+ for a second time, thus measuring the microwave induced population transfer between F^+ and F^-.

The microwave scans were measured with a laser separation of 350 ns during the 2006 beam time. A trial scan with a 500 ns laser separation was also measured, but it was concluded that 350 ns was more statistically significant. Fig. 1.14 shows the 2001 microwave scan next to data that was measured over a period of 12 hours during the 2006 beam time. The new measurement has a preliminarily analysed resolution of 60 kHz (a factor of 5 better than the 300 kHz resolution in 2001) and a line width of 2 MHz (6 MHz in 2001). The line width is determined by the Fourier transform of the microwave pulse due to the short time window in which it is fired.

1.4 $\bar{p}$He – Beamtime Proposal for 2007

1.4.1 PPB-scale laser spectroscopy of $\overline{p}$He$^+$ atoms by sub-Doppler laser spectroscopy – 6 weeks

In 2007, we plan to carry out detailed and systematic measurements of the two-photon transitions in both $\overline{p}{}^3$He$^+$ and $\overline{p}{}^4$He$^+$. These studies are essential in characterizing the systematic errors in these experiments such as collisional frequency shift, power shifts, and AC-Stark shifts, and would immediately lead to an improvement of the known value of the antiproton-to-electron mass ratio. For this purpose, we are currently increasing the intensity and frequency stability of our two pulse-amplified Ti:sapphire lasers, and stabilizing them to a femtosecond optical-frequency comb generator [10, 11]. The higher laser intensity and resolution should improve the signal-to-noise ratio of the two-photon signal by a factor of 5-10 compared to our 2006 results. We intend to measure the two-photon transition at four different settings of the laser intensity, frequency chirp, and offset ΔE between the virtual intermediate and real states.

1.4.2 $\bar{p}{}^4$He Hyperfine Splitting – Proposed Measurements 2007 – 4 weeks

Table 1.3 summarises a journal article, recently submitted to Physical Review A, by Bakalov and Widmann [17]. Δ_q stands for the estimated relative accuracy of the QED calculations. Row δ_μ indicates the absolute accuracy to which various different hyperfine states of antiprotonic helium need to be measured to achieve the current accuracy of the antiproton magnetic moment. The row δ_{exp} indicates the absolute experimental precision required to reach the limit of the accuracy of the theory. The row Δ_q/Δ_μ indicates the improvement factor to the current known precision of the antiproton magnetic moment if one was to measure to the resolution of row δ_{exp}.

	(35,33)	(37,34)	(39,35)	(33,32)	(36,34)	(37,35)	(35,34)	(34,33)	(38,35)
$\Delta_q \times 10^4$	6	11	3	8	23	12	6	4	5
δ_μ (kHz)	180	90	270	510	50	90	210	360	190
Δ_q/Δ_μ	5.0	2.7	8.9	3.6	1.3	2.7	5.4	8.4	6.0
δ_{exp} (kHz)	36	33	30	142	38	33	39	43	32

Table 1.3: *Summary of comparability of measurements between theory and experiment*

Thus measuring the hyperfine structure of the (37,35) state to a resolution of 30 kHz will result in a factor of 3 improvement to the known antiproton spin magnetic moment. It is therefore proposed that a completion of the systematic study that was commenced in 2006 will be made during the 2007 beam time.

A resolution of 60 kHz was achieved in 12 hours. With a reduction and careful selection of measurement points these results can be repeated within 8 hours. Four times the statistics are required to reduce the resolution to 30 kHz. Thus 32 hours are required for one scan. As during each shift about 1 hour is needed for beam tuning and other preparations, it will take 5 shifts to achieve the desired resolution.

A systematic study should examine the density dependence. It is therefore proposed that scans are made at three different densities (150, 250, and 500 mbar). At five shifts per scan, 15 shifts would be required.

In addition, 6 shifts would be required for setting up and optimising the experimental conditions. This process would include ranging, laser scans and microwave on-off, at each density.

Finally, to eliminate systematic errors, it is necessary to make an independent scan at a higher microwave power. To be meaningful this must be taken with the same statistics as the previous scans. A second

additional scan, also to eliminate systematic errors, will be required at a different laser firing time difference. Due to time constraints this will be performed at 150 ns because it has the highest signal to noise ratio and such a scan will take less time. For these two measurements 7 shifts are required.

In total the beam time proposal in 2007 for the hyperfine splitting of antiprotinic helium is 28 shifts (4 weeks). With this time we will be able to publish a measurement of the antiproton spin magnetic moment to a factor of 3 better than it is currently known.

1.4.3   Measurement of the Auger decay rate of $\bar{p}$He$^+$

As described in 1.1, our results for the transition frequencies (ν) of $\bar{p}$He$^+$ agree with the three-body QED theory calculations [3–5] at a level of $< 10^{-8}$, but since our determination of $m_{\bar{p}}/m_e$ rely on the three-body QED calculations, it is important to check the validity of the theory predictions. One way is to compare the $\bar{p}$He$^+$ Auger decay rates (Γ_A^{exp} vs $\Gamma_A^{\mathrm{theory}}$). This is because the transition frequencies and the Auger rates are simultaneously obtained as complex energy eigen values $h\nu - i\Gamma_A/2$ in the theoretical calculations, and hence the theoretical precision of $h\nu$ (real part) and Γ_A (imaginary part) are expected to be of the same order.

Figure 1.15 shows a part of our previous measurement of the Auger rates (having 10-50% relative errors) compared to theoretical calculations [22]. In the previous measurement, we employed two different methods depending on the magnitude of Auger rates. For the slow rate less than ~ 0.2 GHz, we measured the Auger rates by fitting an exponential decay to the tail of the laser-induced annihilation spike. The three states indicated in the figure were measured with this method. For others, we determined the Auger rates from the resonance width, corrected for the laser bandwidth.

As shown in Fig. 1.15, while some transitions show good experiment-theory agreement, large differences were found in some others, especially for the states measured using the "resonance-width" method. One of the reasons for the differences could be the large (a few GHz) bandwidth of the commercial dye
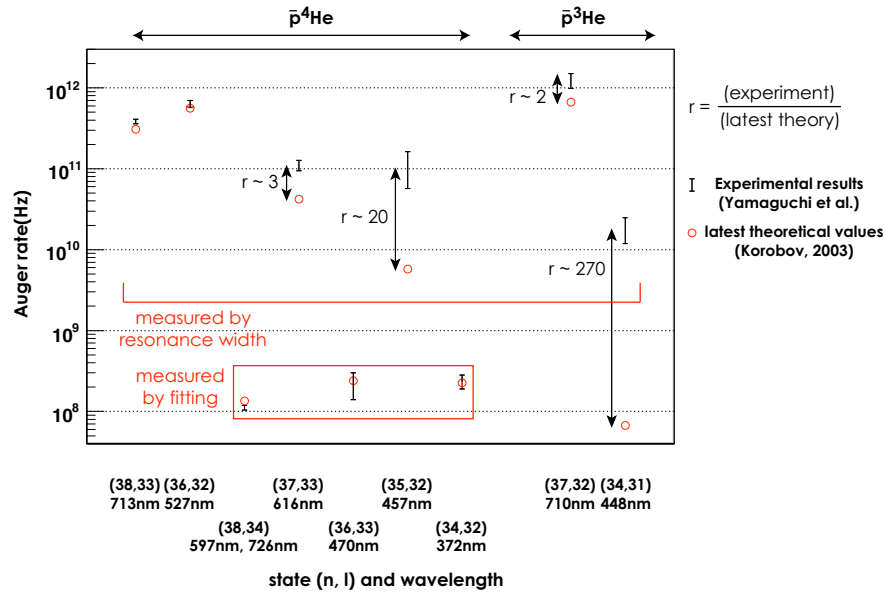
Figure 1.15: *A part of results of our previous Auger rate measurement compared to theoretical calculations [22]. The three Auger rates shown in the lower part of the figure (small Γ_A) were measured by fitting an exponential to the laser-induced resonance spike, while others were measured by their resonance widths. As shown, experimental results and theoretical predictions agree fairly well for some transitions, while there exist factor 2-270 differences in some others.*

lasers used in those measurements. When the laser bandwidth is comparable to the natural width, it was difficult to derive the Auger rate. For example, the Auger rate of the state (35, 32) of $\bar{p}^4\text{He}^+$ is predicted to be $\gamma_{\text{nat}} = \Gamma_A/2\pi \simeq 1\text{GHz}$, which was close to the linewidth of the previously-used laser system.

We propose to perform a new series of measurements with the continuous-wave pulse-amplified laser system which was successfully used for the high precision spectroscopy of $\bar{p}\text{He}^+$. The bandwidth of the new laser is about 50 MHz, which is a factor > 20 smaller than the previous one. With enough statistics, we can measure the Auger rates with less than 5 percent relative errors, an improvement of a factor $2 - 10$ over the previous measurements.

Since the experimental apparatus is same as the magnetic moment measurement, the Auger-rate measurement can be done parasitically, without requiring an additional beamtime allocation. In 2007 we plan to measure the states (38, 33), (36, 32) of $\bar{p}^4\text{He}^+$ and (37, 32) of $\bar{p}^3\text{He}^+$. The studies of (37, 33), (35, 32) of $\bar{p}^4\text{He}^+$ and (34, 31) of $\bar{p}^3\text{He}^+$ require some laser development work, and will be carried out in 2008. The state (36, 32) of $\bar{p}^3\text{He}^+$, which has not been measured so far, will also be measured.

Part 2

Atomic/Nuclear Collisions using Slow Antiprotons

2.1 MUSASHI Commissioning

The MUSASHI sub-group of ASACUSA collaboration has been developing a monoenergetic ultraslow antiproton beam source by combining in series the AD (5.3 MeV), the RFQD (Radio-Frequency Quadrupole Decelerator, 50–120 keV), and a MRT (multi-ring electrode trap, ~ 0.1 eV) installed in a superconducting (SC) solenoid of 2.5 T. The antiproton cloud was cooled and radially compressed, then accelerated to several hundreds of electronvolts, and transported to two collision chambers with high density gas targets via a transport beamline.

In 2006, a new superconducting (SC) solenoid was installed to improve the reliability and to save manpower, start-up time and time in keeping the magnet in stable condition. We have succeeded in stable operation supplying ultraslow antiproton beams at 250 eV to AIA (Aarhus Ionization Apparatus) for ionization and the supersonic gas jet chamber for antiprotonic atom formation experiments during the run.

Installation of the new magnet

By 2004, we had succeeded in accumulating 1.2 millions antiprotons [30], and extracting half a million of them as an ultraslow antiproton beam and started to supply the beams to ultraslow antiproton collision experiments. However the old superconducting solenoid had a lot of problems, and its stable operation was almost impossible, *e.g.*, the cooling loops of the cold bore tube were often blocked, which prevented us from continuously operating the system, the temperature of the cold bore was unstable, and the consumption of liquid helium was too high.

To solve these problems so that the manpower can be put more to next steps, we designed and constructed a new SC solenoid (Fig. 2.1) cooled by a refrigerator with a maximum magnetic field of 5 T. The bore tube containing the MRT was also cooled by two refrigerators, so the new system is fully automated and liquid helium free. The solenoid is covered with a larger magnetic shield to reduce its leakage field, which helps to improve the transport features of ultraslow antiproton beams and also to improve normal operation of PMTs and Gate valves installed close to the solenoid.

The SC solenoid was delivered to CERN last April. It took 5 days and 1.5 days to cool down the magnet and the bore tube, respectively, which were in accord with its original design.

Test experiments

To evaluate the trapping performance and also to confirm the charged particle handling technique which we already developed with the old magnet, off-line tests were perfomed with electrons and He^+ ions.

Decompression and compression of the cooling electron cloud in the MRT were realized by applying the rotating electric field. Because the initial radius of the electron cloud (~ 1 mm) is much smaller than that of the incoming antiprotons (~ 3 mm), the decompression technique is also very important to effectively cool the incoming antiprotons.

The same compression technique was also applied for trapped antiprotons. In order to efficiently transport antiprotons from the MRT in the SC solenoid to the end of the transport beamline, the radial blow-up of antiproton beam should be less than 25 mm around the extractor electrodes immediately upstream of the first Einzel lens, where the magnetic filed strength is a few milliteslas. According to a trajectory simulation, the antiproton radius in the MRT should be less than 1 mm to fulfill the above condition. As test experiments, He^+ ions were successfully used by preparing and accumulating He^+ ions in the MRT by an electron impact of He gas which was introduced through the transport beamline.

Production of ultraslow antiproton beams

After confirming our plasma handling techniques, we were able to begin work with 111.5 keV antiproton beams from the RFQD. Partly because the number of antiprotons in one AD shot was about two thirds the number achieved in 2004, and partly because of the "strong" stray fields emanating from the 3-T ATRAP2 magnet, we were typically able to trap only 0.8×10^6 antiprotons , of which the number emerging in slow-extraction (i.e. continuous) mode at 250 eV was 1.0×10^5.

The beam profile of the extracted ultraslow antiprotons was measured at the end of the transport beamline
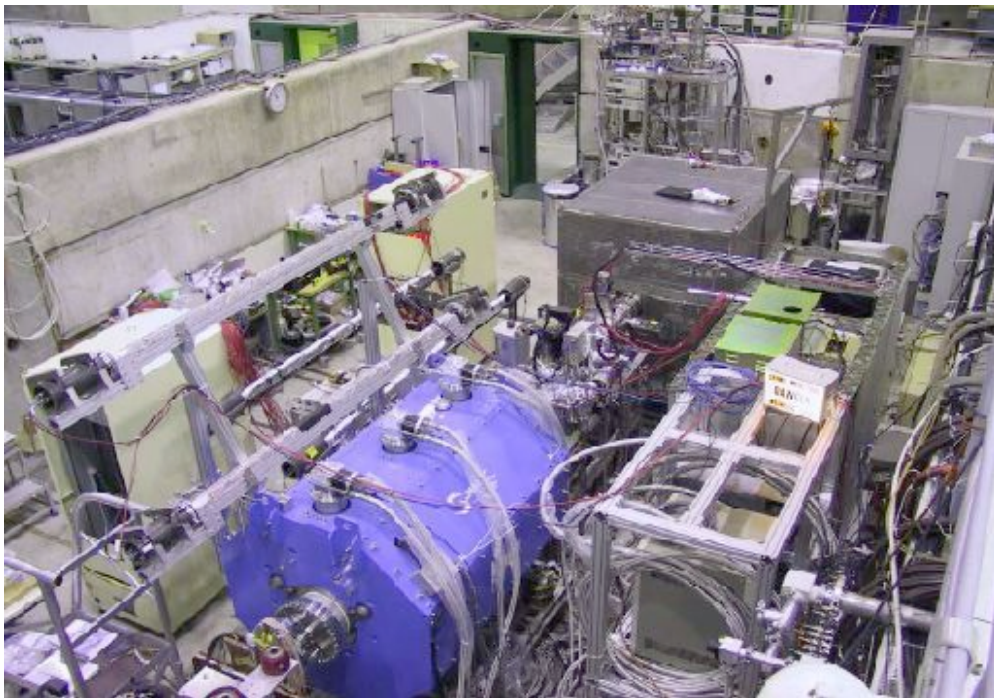
Figure 2.1: *The last part of the ASACUSA beam line, November 2006. In the foreground, the MUSASHI Penning trap can be seen. The square box following it contains the ionization apparatus, AIA.*
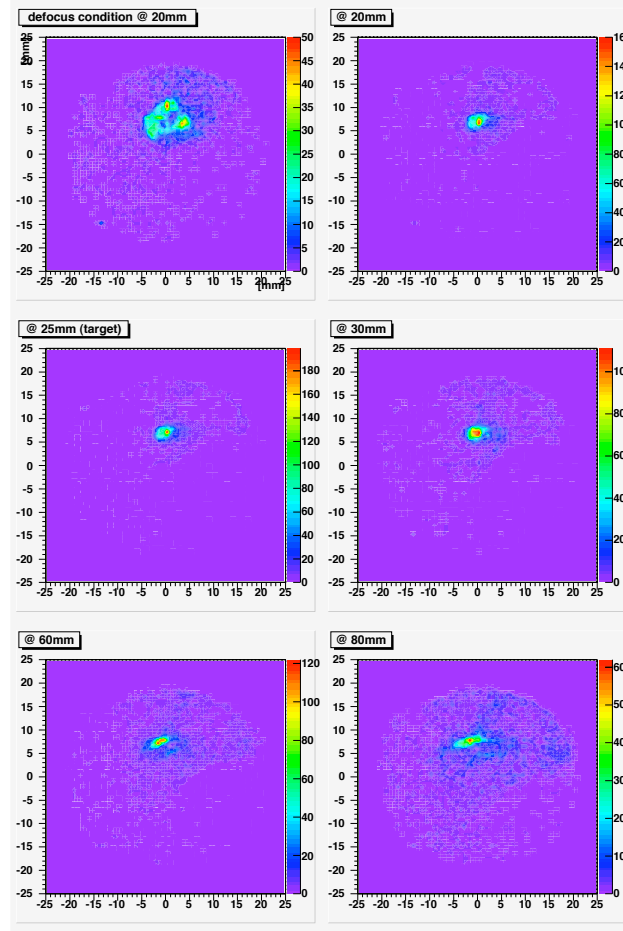
Figure 2.2: *MCP images at the end of the transport beamline.*

(Fig. 2.2) with a 2-dimensional position sensitive detector, MCP-DLD (microchannel plate with delay-line anode detector). Because the MCP activated by antiproton annihilations and gave many false pulses, it was necessary to take coincidence of signals from a scintillator box located close to the MCP-DLD, in order to correctly count the number of antiprotons. The beam profiles so determined were measured upstream and downstream of the target position, 25 mm downstream from the last electrode of the transport beamline to be compared with the simulation. The observed images are show in Fig. 2.2 with the MCP-DLD positions at 20 mm, 25 mm, 30 mm, 60 mm, and 80 mm. It is observed that the beam is well-focused in the range from 20 mm to 30 mm. The beam diameters at the focusing position were 2.5 mm and 1.8 mm in x and y direction respectively, and the diverging angles were $\sim 6°$ and $\sim 3°$.

Slow extraction

Figure 2.3 shows the number of antiprotons counted with the MCP-DLD as a function of time during the extraction by slowly ramping up the bottom potential of the MRT. The potential difference between one of the MRT (V_{MRT}) electrodes forming the barrier and the ground was fixed during the extraction, so the transport energy was also fixed [31]. Antiprotons at 250 eV were extracted from the MRT for more than 8 s to 10 s.

The temperature of antiproton cloud transported to the MCP-DLD was determined assuming the Maxwell
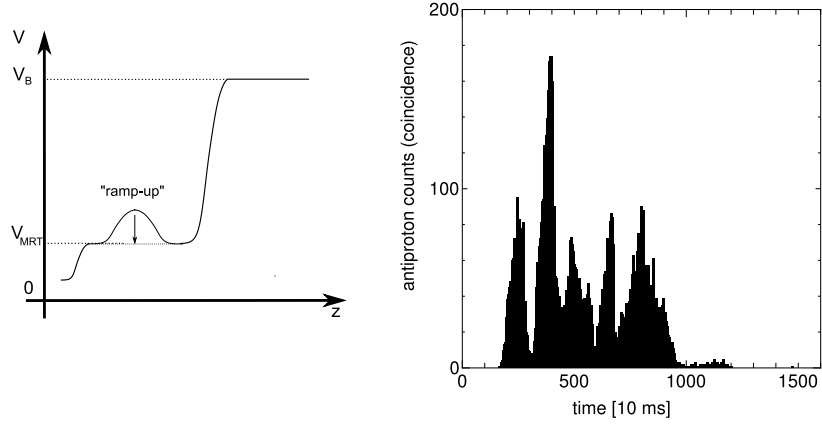
Figure 2.3: *Left : "ramp-up" scheme of the trap potentials for slow extraction of antiprotons. Right: time evolution of the count rate of 250 eV antiprotons counted by the MCP-DLD.*

distribution of antiprotons in the cloud. The number of leaked antiprotons, N, as a function of the potential barrier, ϕ, of the MRT can be fitted by

$$\frac{d\log N}{d\phi} = 1.05\frac{q}{k_B T}, \tag{2.1}$$

which yielded around 0.1 eV as the antiproton temperature, where k_B is the Boltzmann constant, q is the elementary electric charge.

2.2 Status of the $\bar{p}$-atom ionization (AIA) experiment.

Although the basic work by Niels Bohr [23] at the beginning of the last century and the subsequent invention of quantum mechanics permitted the hydrogen atom to be described almost exactly, the three body nature of the helium atom meant that the interaction between its two electrons had to be taken into account in extending this success further . This challenging task was eventually met, in such a way that successive approximations led to a sufficient accuracy, while the basic 3-body problem could not be treated exactly, of course. Later, similar, though less accurate, calculations have been performed for the other atoms.

From the middle of the last century, a new challenge was encountered, namely the "structure" of collisions between atoms and charged particles. Again, Bohr [24] was a central participant in the theoretical development. Such collisions are not static as the atoms, but evolve dynamically, often during time-scales comparable with the revolution times of the atomic electrons. The force on the atomic electrons from a charged atomic particle is of the same order of magnitude as their binding force to the atom, and if the projectile is positively charged, electron transfer is a possible complication. Furthermore, for multi-electron atomic targets, dynamic electron-electron correlation has to be taken into account. For light projectiles such as electrons, scattering complicates matters.

This plethora of challenges means that even today, we cannot claim to have a general theoretical description of charged particle-atom collisions that allows us to calculate even such simple quantities as the total cross section for single ionization. There are some volumes of the parameter space for which the situation is rather satisfying. For example, this is the case for projectiles of low charge and very high velocity colliding with light atoms, where perturbation theory gives satisfactory results for single ionization cross sections. However, it is also necessary to describe accurately collisions outside this parameter space.

For this purpose, our group has chosen to study the special case of antiprotons colliding with light atoms. Here there is no complication from electron transfer and the mass of the projectile allows straight-line
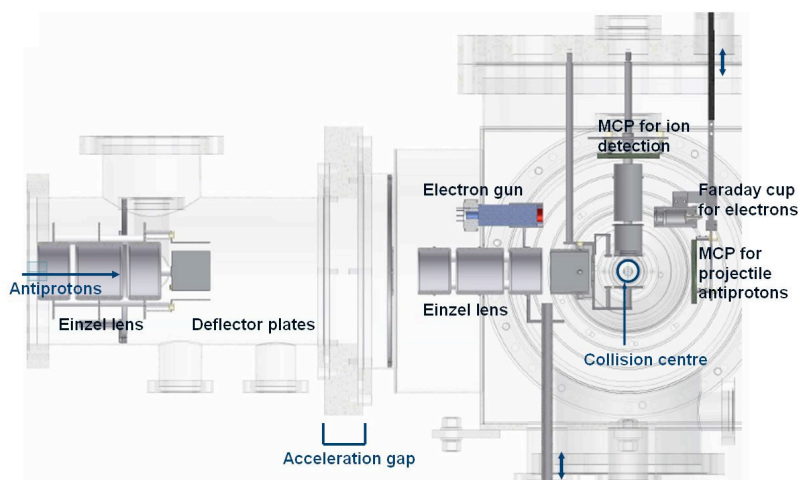
Figure 2.4: *The inside of the AIA, where the antiproton beam crosses a beam of helium atoms. The antiprotons and the created helium ions are detected, and the TOF of the ions deduced.*
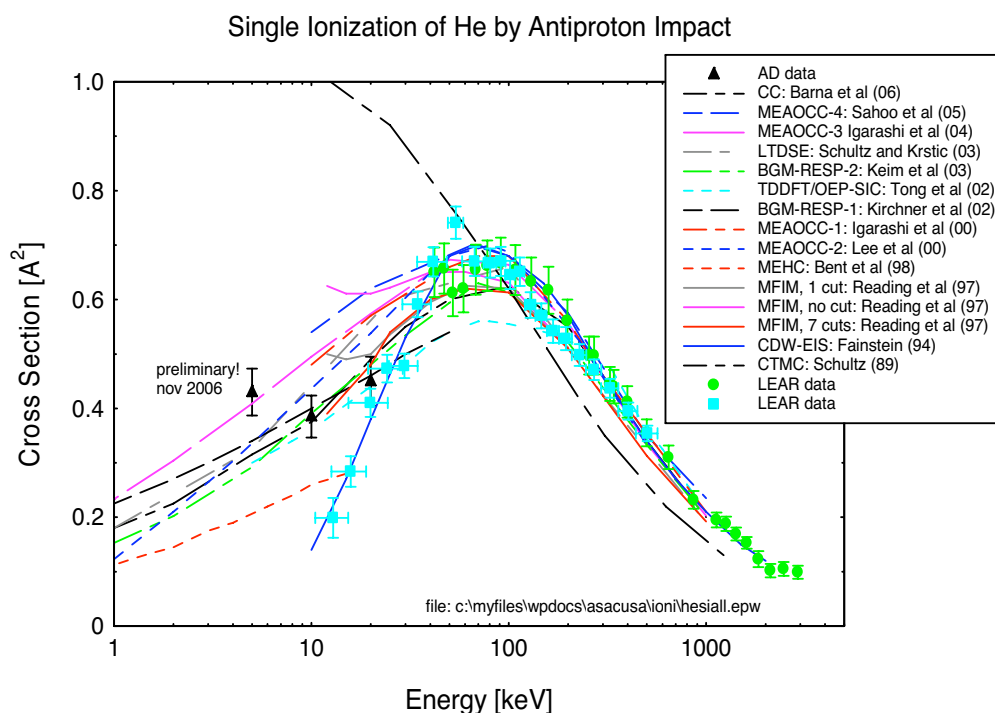
Figure 2.5: *The single ionization cross section for antiproton impact on helium as function of the projectile kinetic energy. The experimental data [28, 29] obtained by our group at LEAR, compared with the new data (preliminary!) and various theoretical calculations.*

trajectories to be used in the models. Already in 1986, this led to a breakthrough in the theoretical treatment of electron-electron correlation in high velocity ionizing collisions [25]. Since then we have supplied the theorists with a large body of benchmark data for their development of proper theoretical models [26].

As our insight into the theory of atomic collisions improves, it has become clear that the challenge now lies in the understanding of "slow" collisions, i.e., collisions where the projectile speed is smaller than that

of the target atoms outer electrons. In the case of antiproton impact, this means antiproton kinetic energies less than a few tens of keV.

During our work at LEAR, we were able to cover the energy range down to 10-20 keV, but a whole new approach to the production of an antiproton beam was needed to go lower in energy. This challenge was taken up by the ASACUSA collaboration, and it has now allowed us to measure the ionization cross sections for energies as low as 5 keV, a World record for antiproton collision cross section measurements.

The new technique involves an RFQ decelerator, which delivers an antiproton bunch at 10-20 keV but with a large energy and angular spread[1]. To overcome this poor quality of the antiproton beam, the MUSASHI group of ASACUSA has developed a superconducting Penning trap with an associated extraction beam line. Here, the antiprotons are captured, cooled, compressed and finally extracted as a beam of a few hundred eV. This constitutes a major achievement, and opens the possibility of a plethora of new investigations of the structure of antimatter, the interaction of antimatter with matter as well as of atomic collisions with very slow antiprotons.

Using this facility connected to our ionization apparatus AIA, we have performed measurements of the single ionization of helium for impact of 5,10,15 and 20 keV antiprotons. The experimental setup is shown in figure 2.1.

Figure 2.4 shows the inside of the AIA vacuum chamber. After passing the first Einzel lens, the $\sim$ 250 eV antiprotons are accelerated into the rest of the apparatus, which is floating on a positive high voltage corresponding to the required collision energy. They are then focussed onto a beam of helium atoms and then they are detected by a large MCP detector. The ions created are extracted onto another MCP. The time difference between pulses in these detectors gives the ion time-of- flight (TOF). The product of target density, target length and ion detector efficiency is determined using a 3 keV electron beam, which can be placed in the path of the antiproton beam. Here, well known electron ionization cross sections serve as normalization. Figure 2.5 shows a comparison between our new data (which are not yet finalized!) and the former data of our group.

As can be seen, the theoretical calculations are more or less in agreement for fast collisions (energy> 100 keV) while they show a large spread for slow collisions: For 10 keV impact energy, for example, the theoretical spread is $\sim$ 30% (!). This shows the need for benchmark data in this region. However, the experimental data by [28] show an energy dependence quite dissimilar to any of the theoretical calculations. It was pointed out often in the past that the two lowest data points might be erroneous.

With our new results from the 2006 run, we can state that this is probably so, and that the gross energy dependence of most of the theoretical calculations is correct. This solves an outstanding problem in this field.

In addition to the helium data, we also obtained similar data on argon as a target, but these results await a proper data analysis.

2.3   Ionization and atomic capture processes between an ultra-slow antiproton and an atom

The ultra-slow antiproton beam which can now be extracted stably from the MUSASHI apparatus at energies of the region of atomic physics, has opened up the possibility to study ionization and atomic capture processes between a very slow monoenergetic antiproton and an atom under the single-collision condition for the first time. Studies of ionization cross sections at relatively high energies of 5–20 keV has been mentioned in section 2.2 with their successful results. Studies of ionization and atomic capture processes at

---

[1]With the beam from the RFQD, we have nevertheless been able to perform an important series of measurements of the energy loss of slow antiprotons passing through thin foils, see e.g., [27] However, in this case we measure an integral quantity, which includes all ionization and excitation channels, and which can be treated theoretically with "simpler" models.
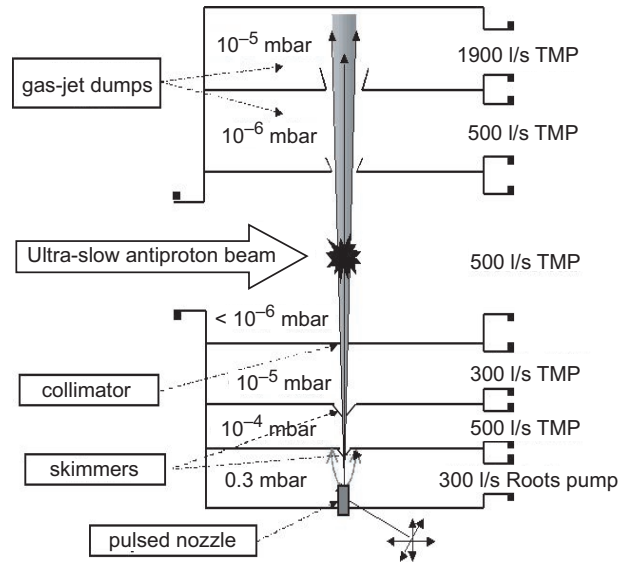
Figure 2.6: *Schematic design of our supersonic atomic gas-jet target.*

lower energy than 250 eV uses another dedicated gas-jet target system and a different particle detector set, which will be explained below.

We performed some test measurements at the end of our beamtime in 2006, and obtained promising results despite the too short beamtime of only 4–5 effective shifts of 8 hours. We will continue this experiment to study atomic capture of antiprotons and formation of exotic antiprotonic atoms.

Aim of the experiment

The antiproton is a unique probe for atomic physics research. It behaves as a heavy electron or as a negative nucleus and gives a new test ground for studies of atomic collision dynamics. It is a "theoreticians' ideal projectile" because lack of electron capture processes avoids complication in theoretical treatments, and some theoretical work is going on [32]. Yet so far no experiment was possible at energies less than around 20 keV. With the advent of our ultra-slow antiproton beams at 10–250 eV, ionization and atomic capture processes of an antiproton projectile against various atoms "A",

$$\bar{p} + A \rightarrow \bar{p} + A^+ + e^-$$

$$\bar{p} + A \rightarrow (\bar{p}A^+)^0 + e^-$$
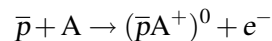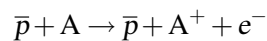
can be studied for the first time under the single-collision condition. This study also reveals the properties of exotic antiprotonic atoms formed in vacuo.

Atomic gas-jet target

Atomic collision experiments requires an atomic gas-jet target to be crossed with the antiproton beam. We prepared a supersonic gas jet in order to have a possible maximum density of the target to obtain reasonable reaction rates of ionization and atomic formation processes. Helium atom was chosen for our first target, for technical simplicity and because of the fact that the lifetime of antiprotonic helium atoms are already known from our previous spectroscopic measurements [33].

We developed a gas-jet system with 6 chamber stages, in collaboration with a gas-jet specialist over a few years (see Fig. 2.6) [34]. A supersonic gas jet emerging from a 0.1-mm-diameter nozzle was skimmed
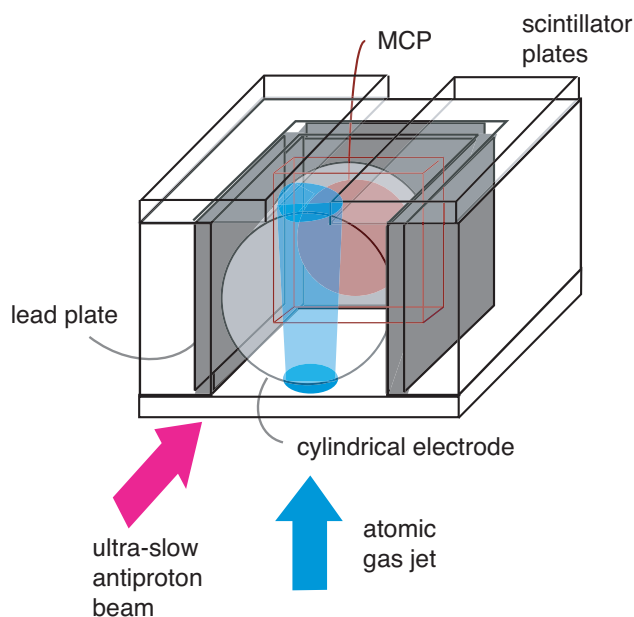
Figure 2.7: *Schematic setup of detectors surrounding the collision point of the antiproton beam and the gas-jet target.*

by two stages of skimmers and collimated to form a jet of 1 cm diameter at the cross point in the main chamber. The jet was collected by powerful turbomolecular pumps at the dump stages with an over-90% efficiency and the vacuum in the main chamber was kept to a level of less than 10^{-6} Torr. Three apertures and differential-pumping stages along our 3-m beamline for antiproton extraction guaranteed the vacuum of the antiproton trap region to a level of less than 10^{-12} Torr required for stable antiproton storage free from annihilation [31].

Detection and data acquisition systems

Antiprotons, about 10^5 in number, were extracted in a slow-extraction mode over a period of typically 10 seconds. This continuous beam allowed event-by-event data acquisition associated with each single antiproton extracted. For particle detection, a microchannel plate (MCP) with a two-dimensional position sensitive detector was placed 6 cm downstream of the antiproton beam from the cross point, and was surrounded by a box of lead plates and scintillator plates (see Fig. 2.7). An antiproton impacts a helium atom and ionizes it, emitting an electron, which is then guided by a cylindrical electrode toward the MCP with an efficiency larger than 90%. Depending on the impact energy, the antiproton either travels downstream at a lower energy or is captured to form an antiprotonic helium atom which flies at an even lower speed toward downstream. The MCP is used to detect any of these particles: an electron, a bare antiproton, or an antiprotonic atom; while the scintillation counter records antiproton annihilation with 99.7% efficiency by detecting passage of its annihilation products such as pions. The reaction event is recognized by an electron signal (*i.e.* MCP hit and no scintillator hit) followed by an antiproton signal (*i.e.* both MCP and scintillator hit) with an appropriate TOF (time-of-flight) interval.

2.3.1 Antiproton beam trajectory

Designing the beam transport of ultra-slow antiprotons is not a trivial task at this very low energy. The antiproton beam needed to go through 3 aperture stages along the 3-m extraction beamline before it was
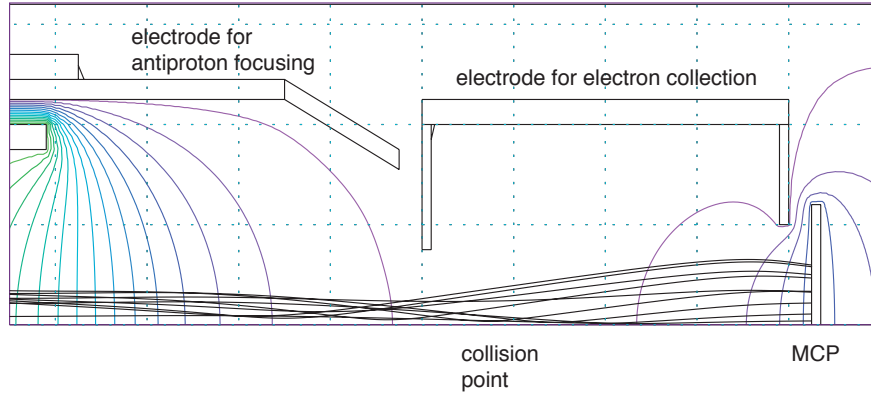
Figure 2.8: *Simulated antiproton trajectoris at 250 eV at the last stage of the beamline. The antiproton is well focused near the cross point to overlap the gas-jet target while the beam divergence is kept small enough for the beam to be detected within the sensitive area with a 4-cm diameter of the MCP placed 6 cm downstream.*
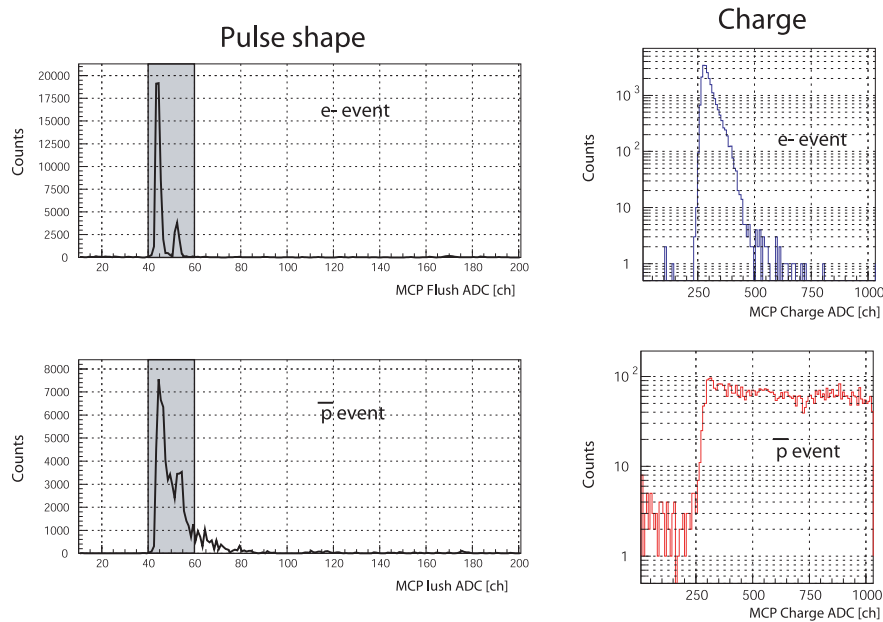
Figure 2.9: *Left: Averaged time structure, recorded by a flash ADC module, of the MCP signals for electron and antiproton incidence show clear difference. (One channel corresponds to 10 ns for the horizontal axis.) Right: Histograms of integral charge of the signal are shown. This charge information can be used for particle discrimination and helped suppress background events.*

focused at the collision point. The last focusing had to fulfill two contradictory conditions: the beam spot must be squeezed to the small size of the gas jet, yet the focusing has to be weak enough to keep the beam divergence to a small value so that all the antiprotons and antiprotonic atoms should be collected at the sensitive area of the MCP downstream. Figure 2.8 shows a solution to the simulation of antiproton trajectories at 250 eV, from the last stage of our beamline through the collision point against the gas-jet target, until the MCP downstream. The MCP was biased at $+470$ eV to draw in the negative particles. The beam size was squeezed to a diameter of 8 mm at the waist, to ensure a good overlap with the gas jet.

2.3.2   First results

Within the limited beamtime allocation of 4–5 effective shifts, we managed to re-tune the ultra-slow antiproton beam, adjust our detection systems and take first test data. The experimental antiproton trajectory was in agreement with the simulation, judging from the beam spot image observed by the MCP. During the course of the detector adjustment, we found that the MCP signals for electrons and antiprotons have significantly different shapes, as shown in Fig. 2.9. (To our knowledge, nobody has so far investigated signals of ultra-low energy antiprotons impacting onto an MCP, and this is our first finding.) This resulted in a 6 times reduction of background events originating in missed recognition of antiproton annihilation. We also leant that radioactivation of the MCP due to antiproton annihilation on its surface was negligibly small after a time scale of a few hundred nanoseconds, so that it does not contribute to a fake electron trigger signal. The observed TOF spectra taken for antiprotons at 250, 100 and 30 eV show identified electron signals and proves that our strategy and our system are working fine. However, these signals persist even for data without the gas jet, and we suspect the vacuum along the last stage of the beam line is worse than our estimation. The observed signals may originate in ionization of background gases, and we will need to modify the design of the electrodes to allow better pumping of this region in preparation for our coming experiments. The TOF spectra after several selectional cuts of events seem to contain a possible candidate of the reaction peak associated with the gas jet, but the statistics of the data accumulated only for several hours in total is too poor, and we need more careful analysis and interpretation of the data in view of our measurements in 2007.

2.4   Antiproton-nucleus annihilation cross section at low energies

In 2006 we used the experimental setup shown in Fig.2.10 in order to investigate the mass-number dependence of the $\bar{p}$-nucleus annihilation cross sections at 5 MeV.

The foreseen measurement strategy is now described. The $\bar{p}$ beam from the AD is focused on the entrance window of a cylindrical vessel (2 m long, 20 cm in diameter) containing gaseous target. The $\bar{p}$-annihilation products (mostly charged pions) are detected by a Scintillating Fiber Tracker (see Fig.2.11) which is able to reconstruct the annihilation vertex when at least two of the outgoing charged mesons are tracked. Particular attention has been paid in order to avoid background signals coming from the $\bar{p}$ annihilations on the entrance and on the end of the target vessel: 1) Antiprotons from AD cross only thin material (75 micron of Kapton, 50 micron of Mylar) before entering the target. 2) The data must be acquired in a small time gate (about 30 ns) after the last antiproton enters the target and before the first antiproton arrives to the end wall. That is possible when the AD antiproton cloud lasts 30 ns (taking into account the limitation on the target length of only a few meters) . This is why we asked to the AD operations team for multiple extraction with reduced time duration of each extracted $\bar{p}$ cloud.

The $\bar{p}$ beam is counted on the end wall of the target vessel by a proximity focused Hybrid Photo Diode (HPD) which is a linear device with a wide dynamic range and gain proportional to the high voltage applied.

The gaseous target pressure ($1 - 100$ mbar) is tuned in order to have few annihilations events per $\bar{p}$ bunch. The good time resolution (~ 3 ns) of the detector will permit to disentangle tracks coming from different annihilation vertices. We acquired data on 5th-14th September . Due to SPS or AD problems only 60 percent of the beam time was delivered to our experimental zone.

The 2006 antiproton beam did not fulfil the requests for the measurement. While the variations on the beam intensity in the six spill of the multiple extraction resulted acceptable, the existence of a low intensity beam before the main beam affected the measurement deeply. Also the dimension of the beam on the entrance was too large. In Fig.2.12 the time distributions of the particles from antiproton annihilations are shown for a typical run. The measurements correspond to different detectors with different signal amplitude gain and placed in different positions (the Cerenkov detector and the 2 scintillators besides the entrance of

the target, while the HPD at the end of the target). The width of the main bunch results to be around 40 ns, but the whole time range for the incoming antiprotons is greater than 400 ns. These "pre-bunch" caused the selected time acquisition gate to be interested by a flux of pions coming from the end of the target. In addition a beam halo produced a not negligible number of annihilations at the entrance of the target which blinded our position detector for some hundreds of nanoseconds before the arrival of the main bunch to the fiducial volume. Despite many on- and off-line attempts to reduce the background in the 2006 data, it is not easily possible to extract annihilation cross-sections from them. Furthermore, difficulties have been encountered in relating the number of events to the corresonding number of incoming antiprotons.

In Fig.2.13 the time distribution of the hitted fibers of the tracking detector is plotted, showing a temporal superposition of the arrival signals which prevents to disantagle the tracks coming from different annihilations vertices.

The used targets are H_2, D_2, ^4He, ^3He, Ne, Xe.

In Fig.2.14 an event with 2 mesons is shown. The vertex appears near the wall at the target entrance

2.5 Atomic/Nuclear Collisions – Beamtime Proposal for 2007

2.5.1 MUSASHI commissioning — 2 weeks

We successfully launched the new SC solenoid during the 2006 beam time and supplied 250 eV monoenergetic ultraslow antiprotons to two collision experiments. With the experience obtained during the last MUSASHI commissioning, we will further improve the trapping and extraction efficiency by optimizing various parameters such as the magnetic field of the SC solenoid, MRT potential depth, etc. Extraction at lower energies down to 10 eV, will be developed in 2007 for the $\bar{p}$A formation experiment.
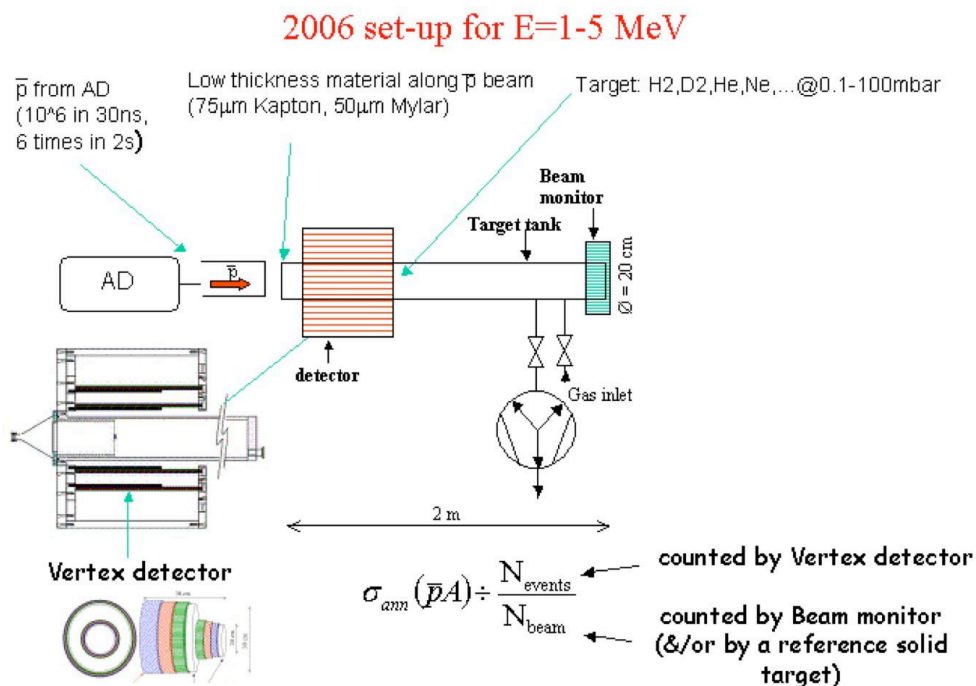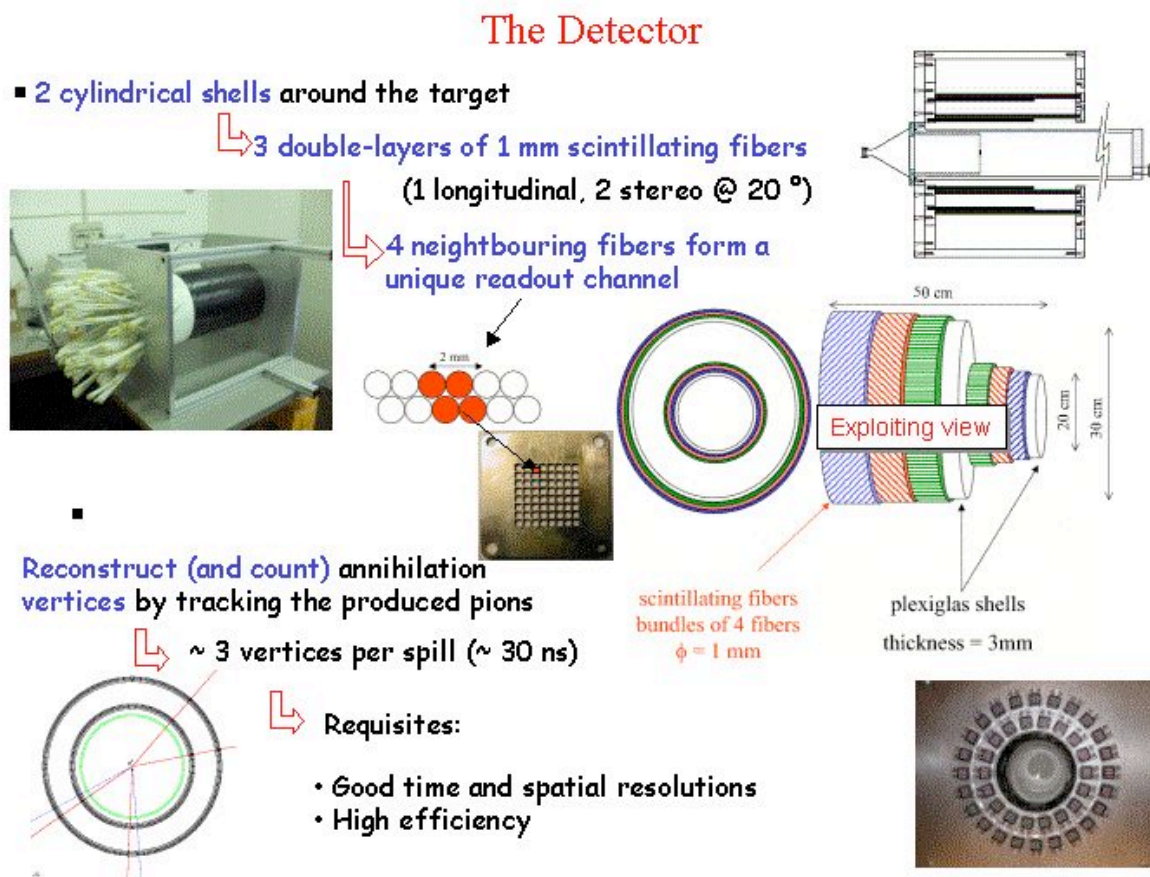

Figure 2.10: *A schematic layout of the $\bar{p}$-A annihilation cross section measurement in 2006.*

Figure 2.11: *The scintillating-fiber detector system used for the $\bar{p}$-A annihilation cross section measurement.*

The fast extraction scheme will also be developed in 2007 for antihydrogen ground-state hyperfine spectroscopy. This development is necessary for an efficient injection of ultraslow antiprotons to the cusp trap.

2.5.2   Ionization – 2 weeks

As can be seen from figure 2.5, the data obtained in 2006 can answer the question about the energy dependence, but they are not accurate enough to allow us to discern amongst the various calculations. It is our plan, in 2007, to measure this cross section to an accuracy which is a factor of two-three times better. We believe that this can be done, since the new data in figure 3 were obtained during 4 shifts. In 2007 we will have more time (even allowing for setup and beam tuning). Furthermore, there are a number of improvements which we expect to give us a factor of ∼two more antiprotons:

The AD intensity was weaker in 2006 than in 2004 and the AD cycle was longer than in 2004. It should therefore be possible to obtain more antiprotons pr. shift from the AD.

With the experience obtained in 2006 it should be possible to improve the MUSASHI trapping and extraction efficiency.

As mentioned elsewhere in this report, the MUSASHI group is now able to extract ∼ 100.000 antiprotons for each 3 AD shots. However, we detect only ∼ 30.000. We know now that the first Einzel lens in AIA
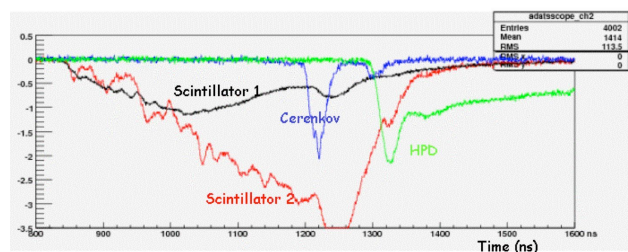
Figure 2.12: *In 2006, we found that each antiproton pulse extracted from the AD is preceded by a small-yet-non-negligible number of antiprotons, making it difficult to perform the annihilation measurement in the original scheme.*
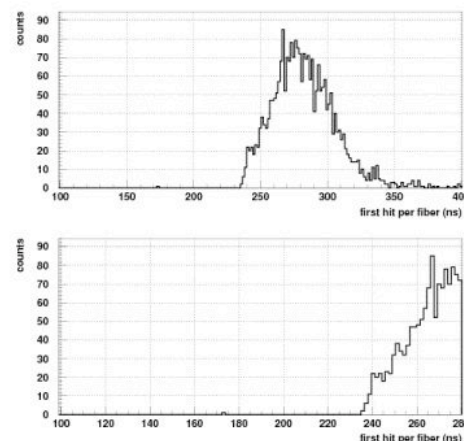
Figure 2.13: *Upper: time distribution of the first hit per fiber. Due to the fact that after an hit each fiber channel remains blinded for 150 ns, the high pions flux-rate causes almost all fibers be still blind after 350 ns. Lower: an enlargement of the initial region of the same.*
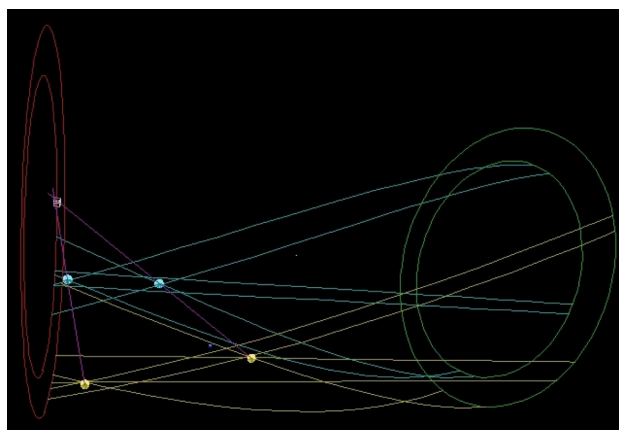
Figure 2.14: *A typical event reconstruction result. The event shown here shows two charged meson tracks.*

is completely filled by the antiproton beam. We will replace it by a larger one. The design and trajectory simulations for this new lens will be fully integrated with the exit lens system of the MUSASHI system. This alone could therefore give us a factor 2-3 more antiprotons.

Furthermore, since we now know that the single ionization cross section is decreasing slowly with decreasing antiproton energy, we should be able to measure down to 2 keV impact energy.

2.5.3 $\bar{p}$+He collision cross section between 10–250 eV – 2 weeks

As was explained in section 2.3, we are about to open up a new field of atomic collision studies with the MUSASHI ultra-slow antiproton beam. The detection and the data acquisition systems are now working, and particle identification of electrons and antiprotons was proven to be good enough for sufficient suppres-

sion of fake trigger events. In 2007, we will improve the vacuum condition to make sure that the electron signals due to ionization of background gases should not disturb our measurements. Antiproton beam transport needs further optimization, and an efficient extraction at energies down to 10 eV must be realized for measurements of the formation cross section of antiprotonic atoms. We will concentrate on measurements with helium target, and accumulate data on ionization and atomic capture cross sections for different antiproton energies ranging from 10 to 250 eV, to clarify collision dynamics between antiproton and atoms for the first time.

2.5.4 $\bar{p}$-nucleus annihilation cross section – 1.5 weeks

The characteristics of the provided antiproton beam from AD impose a different strategy for $\bar{p}$-nucleus annihilation cross sections measurement at 5 MeV.

In Fig.2.15 the new set-up is shown. The detector is the same as in 2006. The main difference concerns the use of solid targets instead of gaseous targets. This will permit to avoid inserting any material, i.e. multiwire chamber and kapton and Mylar windows, between the AD beam line and the solid target sparing the background on the flange due to the beam halo. The tube connected to AD will be about 3 m long and the annihilations of the "pre-bunch" on its end wall will be shielded by about 1 m of concrete.

The target will be few micron thick depending on the used material in order to have about 1 annihilation event per bunch. We will use carbon, silicon, silver and gold deposited with sputtering technique on a few-micron foil of Mylar. The targets can be inserted and removed without opening the beam line.
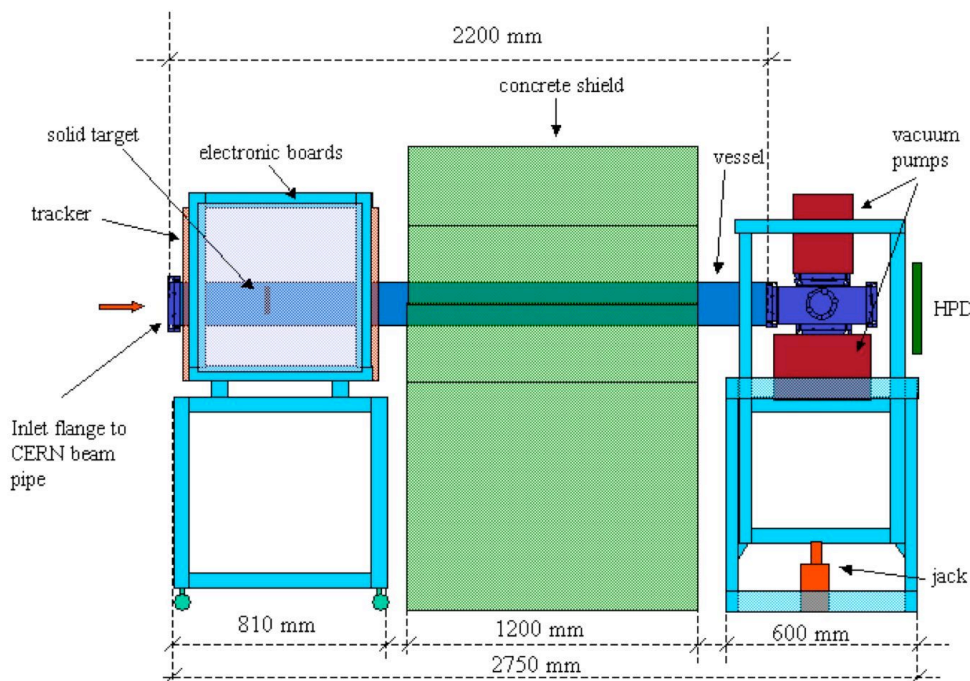
Figure 2.15: *In 2007, we will measure $\bar{p}$-A annihilation cross sections on solid targets (instead of gaseous targets tried in 2006). Background will be significantly reduced as compared with the 2006 measurements by (1) eliminating the entrance window, and by (2) the reinforced shielding against annihilations occurring on the exit flange.*

Part 3

Progress Towards Antihydrogen Ground-State Hyperfine Spectroscopy

3.1 Development of the Paul trap

As explained in reference [35], ASACUSA aims to produce an ultra-slow beam of ground-state antihydrogen atoms which will be used to carry out microwave spectroscopy of their ground-state hyperfine structure. To this end the ASACUSA collaboration continued in 2006 to develop and construct the two radio frequency Paul traps which will be needed to confine the antiprotons and cool them to the temperature required for recombination to antihydrogen atoms. Some of the milestones that have to date been achieved are described below.

First successful demonstration of a cryogenic superconducting RF cavity operating at 30-MHz-scale frequencies and MV/m-scale fields.

We constructed a superconducting RF cavity made of high-purity niobium (Fig. 3.1) using advanced electron-beam welding, vacuum brazing, and surface cleaning techniques. By placing the cavity in a liquid helium cryostat, cooling it to temperature $T = 4.2$ K, and exciting it with a high-power amplifier, we achieved the nominal RF field needed to trap antiprotons. To our knowledge, this is the first time a superconducting
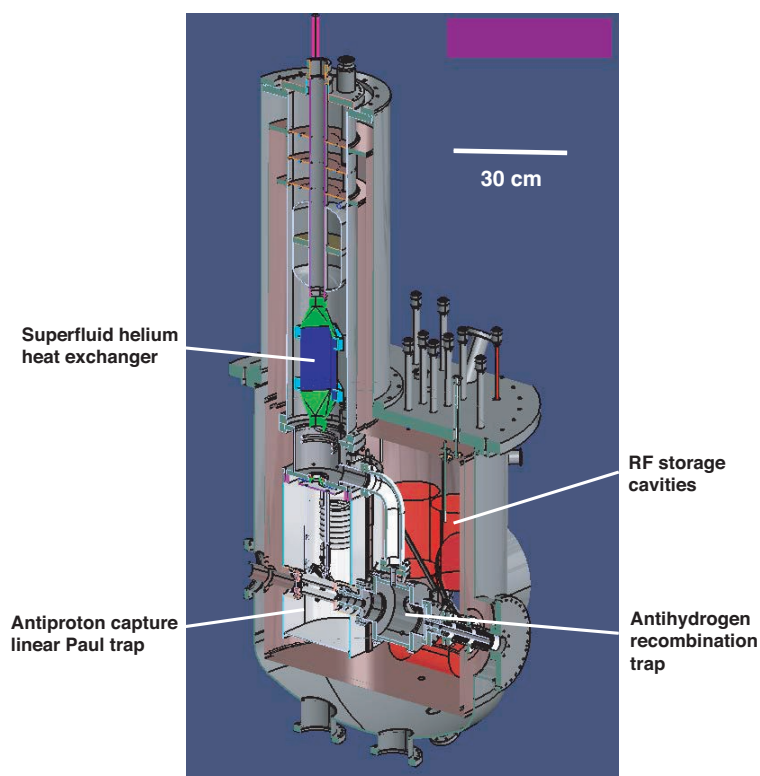

Figure 3.1: *Cryogenic superconducting niobium test cavity being cleaned by water jet and assembled in a clean room at CERN.*
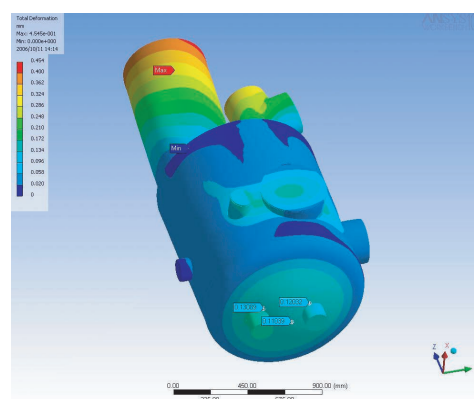
RF cavity has been operated at the 30-MHz range with such a high field; most previous superconducting cavities work at much higher (200 MHz to several GHz) frequencies. Effects due to multipactoring (i.e. resonant discharge between the cavity surfaces leading to a breakdown of the superconductivity) and microphonic vibrations (caused by liquid helium bubbles vibrating the cavity walls and perturbing the resonance frequency), which could in principle compromise the performance of the cavity, were found to be small. This success validated the basic design of the superconducting Paul trap, and allowed us to proceed to the next step of manufacturing the final trap which will confine antiprotons.

Completion of the Paul trap design, and start of manufacture

In Fig. 3.2, a 3D cross-sectional drawing of the two superconducting Paul traps are shown. All technical details have been fixed after careful considerations, simulations, and consultations with CERN experts. Some of these details include a vacuum chamber compatible to a pressure $P < 10^{-12}$ mb, a cryogenic system which cools the traps to 1.8 K, low energy antiproton and positron transport beamlines, and the superconducting RF systems. For example, a mechanical simulation (Fig. 3.3) was carried out to determine the optimum construction of the 1-m-diam vacuum chamber, such that the mechanical deformation in each vacuum port when evacuated would be minimized The Paul traps, including all vacuum and cryogenic systems, are now being constructed. We plan to carry out the first tests with particle trapping in 2008, after extensive cryogenic and RF tests.

Figure 3.3: *Mechanical stress simulations on the 1-m-diam Paul trap vacuum chamber*

Figure 3.2: *Schematic drawing of two radiofrequency Paul traps now under construction.*

## 3.2 Status and plans for the antihydrogen synthesis with the cusp trap

The cusp trap has been developed to synthesize spin-polarized cold antihydrogen atoms in the ground state. The cusp field is obtained by a set of anti-Helmholtz coils, which allows a minimum-B field configuration still keeping axial symmetry. This axial symmetry ensures the conservation of canonical angular momentum of trapped particles around the field axis, which guarantees long confinement time of charged particles (antiprotons and positrons). It is noted that such a feature is quite unique for the cusp trap among neutral particle traps having other minimum-B field configurations, where charged particles like antiprotons and positrons are not stored stably because the magnetic fields used are not axially symmetric. Numerical study also predicts that rigid-rotor equilibrium does exist in the case of the spindle-cusp configuration, though little is known experimentally.

To generate strong cusp magnetic field, a superconducting quadrupole magnet was prepared. The maximum field on the axis is 3.5 T with a large field gradient (38 T/m at maximum). The magnet is equipped with a cryogenic pump system and does not need liquid helium, and has been operated quite stably. A multi-ring trap (MRT) was adopted so that it can generate various electric fields, e.g., a superposition of an octupole field and a quadrupole field.

Status of Preparation

Antiprotons stored and cooled in the MUSASHI trap will be transported to the cusp trap through a magnetic guiding duct of about 0.05 T as a blob. The blob is transported in the magnetic guiding duct keeping its orbital magnetic moment, and can enter the cusp trap having nearly the same magnetic field strength as that of the MUSASHI trap.

Figure 3.4 shows the cross-sectional view of the MRT (a), and profiles of magnetic field and electric potential strength profiles (b and c). Charged particles are trapped by the combination of the cusp magnetic field and electrostatic potential. The set of anti-Helmholtz coils generates the cusp field expressed by the vector potential as $A_\theta(r,z) = (B_0/L)rz$ in the cylindrical coordinates (r,q,z). The cusp magnet constructed can yield the magnetic field as strong as 3.5 T at $z = 150$ mm. In the confinement region of the MRT, the
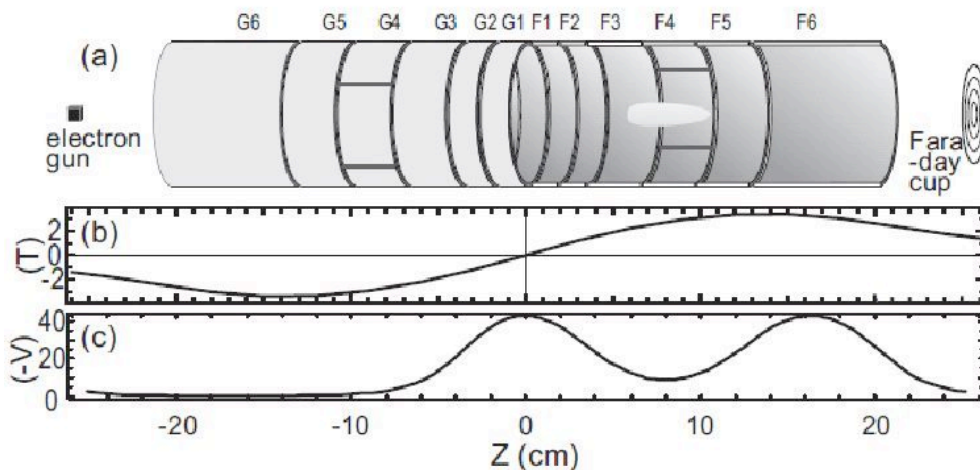
Figure 3.4: *(a) A schematic view of the MRT electrodes and confined plasma. Rotating wall RF fields can be applied from the electrodes G4 and F4. (b)Magnetic field profile and (c) electrostatic potential profile in the electron confinement phase.*
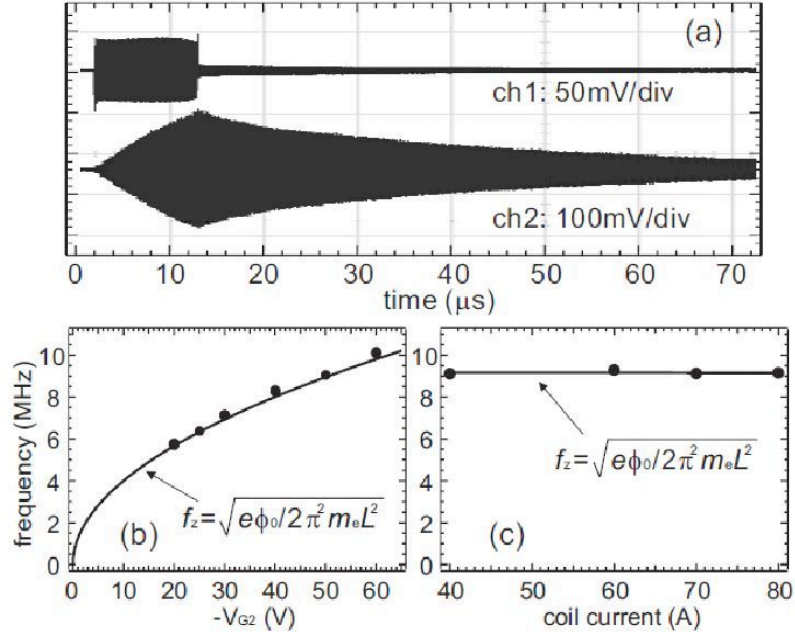
Figure 3.5: *(a) Response of plasma to the external longitudinal RF electric field at the resonance frequency. Ch1: External RF (8.9 MHz) applied on F5, Ch2: excited fluctuations on F3. (b) and (c) Oscillation frequencies of the Eigenmodes as a function of the electric potential and the magnetic field, respectively.*

typical field strength is 1.5 T and the corresponding cyclotron frequency of electrons is 42 GHz.

The scenario to synthesize antihydrogen atoms is the following: Electrons are preloaded in a spindle cusp region $(z > 0)$ of the cusp trap and automatically cooled via synchrotron radiation. Positrons are also loaded in the other side of the spindle cusp region $(z < 0)$. When antiprotons are injected, they are sympathetically cooled through collisions with the trapped electrons. The trapped positrons are kicked into the antiproton cloud, and antihydrogen atoms are synthesized. As is shown below, the radial distribution of the positron cloud can be compressed, i.e., the overlap between the antiprotons and the positrons can be localized sharply resulting in a needle-like source of antihydrogen atoms. The number of electrons could be reduced step by step before the mixture with positrons if they affect the formation of antihydrogen atoms.

Confinement and control of electron plasma in the spindle cusp region

The longitudinal bounce motion of the electron cloud in the trap is given by $(e\phi_0/2m_e)^{1/2}/\pi L$. where ϕ_0 is the depth of the potential well, L a half of the trap length. Figure 3.5(a) shows the response of the electron plasma which is monitored at F5 when an RF field is applied on F3. Figures 3.5(b) and 3.5(c) show the Eigenmode oscillation frequencies as functions of the electric potential and the magnetic field. The dependence on the electric potential suggests that the observed mode is $\ell = 1$ mode of a spheroidal non-neutral plasma. It is noted that such a clear plasma mode has for the first time been observed for non-neutral plasma in a non-uniform magnetic field. On the other hand, no higher modes $(\ell > 1)$ were found till now, which is in sharp contrast to the case in a uniform magnetic field.

The stability of electrons stored in the spindle cusp was studied by measuring the radial distribution of dumped electrons with the segmented Faraday cup (see Fig. 3.4). Figure 3.6 shows the ratio of the charge detected by the central electrode of the Faraday cup to the total charge on the whole electrodes as a function of trapping time. The solid circles in Fg. 3.6 showed that the electron cloud was indeed stored quite stably and expanded only marginally.
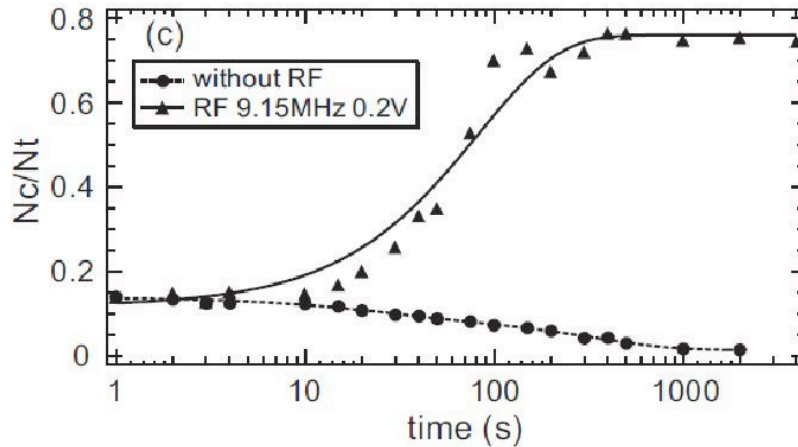
Figure 3.6: *Temporal evolution showing a fraction in the central part of the electron cloud monitored by the segmented Faraday cup (see Fig. 3.4). The solid circles and triangles are the case without and with rotating wall RF field.*

The response of the electron plasma was studied against the rotating wall RF field, which revealed that the plasma radius was compressed when appropriate RF frequencies were selected. Again, this is the first experimental evidence that non-neutral plasma in a non-uniform magnetic field can be manipulated by a rotating wall RF field.

In order to synthesize antihydrogen atoms, positrons on one side of the spindle cusp should be transported to the other side of the spindle region where antiprotons are trapped. Slow leak of electrons to the other side through the $B = 0$ point was tested. The result showed that this operation was easily controlled without causing instability of the electron plasma.
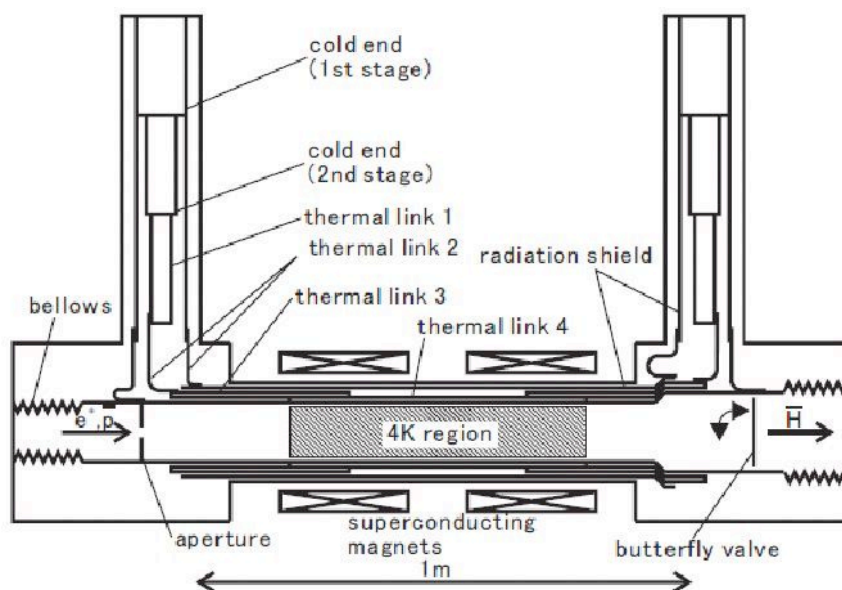
Cold bore of the cusp magnet

Because antiprotons and antihydrogen atoms are quite active against a small amount of residual gases, the MRT region should be kept in an extremely good vacuum, which can be achieved by maintaining the MRT region at a cryogenic temperature around 4K. To realize this, a cold bore that houses the MRT has been designed and constructed. Two cryogenic refrigerators were prepared for the cooling, i.e., the cusp trap is designed to be fully liquid helium free. Figure 3.7 shows the cross-section of the cold bore. It was successfully operated and the bore temperature as low as 4.0K has already been achieved.

Recently, we have also found that the magnetic field configuration of the cusp trap has a high ability to dramatically cool antihydrogen atoms. For example, our simulation predicts that antihydrogen atoms formed in an excited state $(n = 44, m = 43)$ in the cusp trap at 15 K can be cooled down to 400 mK during cascading.

3.3 Status and plans for the ASACUSA positron beam line

During 2006, the first two major parts of the ASACUSA positron beam line were ordered from First Point Scientific, California, USA. The layout of the beam line is shown in figure 3.8.

The entire apparatus consists of 3 parts: The RGM-1, in which positrons emanating from a ^{22}Na source are moderated by solid neon and extracted (see figure 3.9), an accumulation and cooling buffer gas Penning trap where the positrons are cooled to room temperature (see figure 3.10), and finally a stacking, compression and bunching Penning trap for the final manipulation of the positron beam.
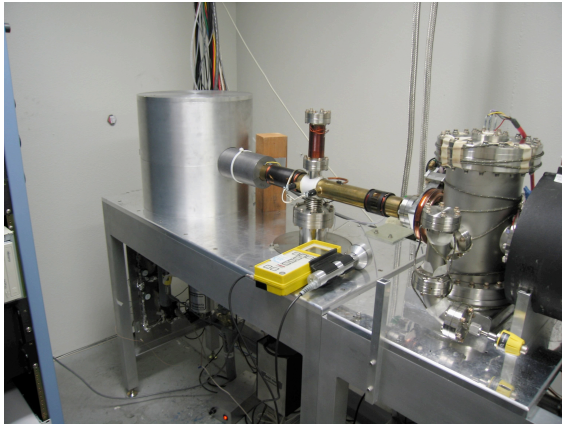
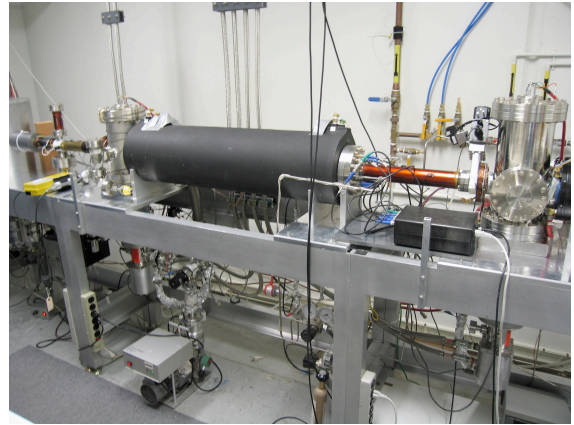**Figure 3.7:** *A schematic drawing of the cold bore installed in the cusp magnet.*
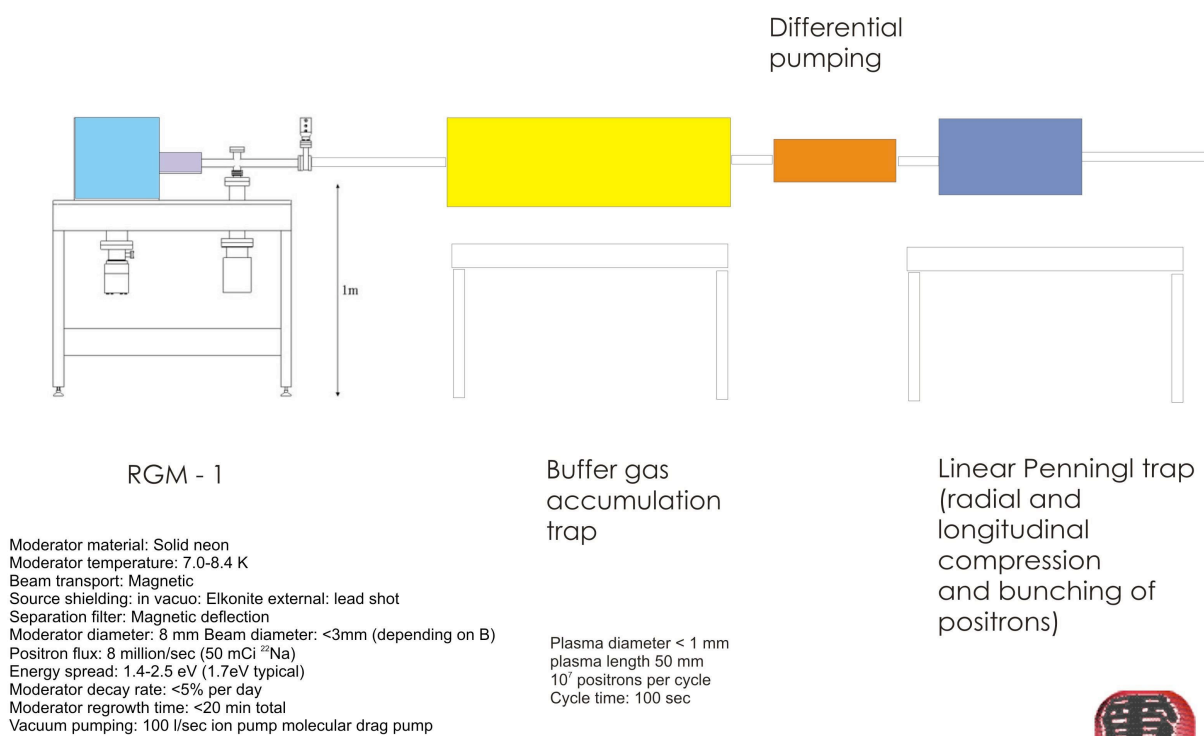
Figure 3.8: *The schematic layout of the ASACUSA positron Beam line.*

Figure 3.9: *The RGM-1.*

Figure 3.10: *The Buffer gas Penning trap.*

The first instalment of the RGM-1 has been paid and the entire RGM-1 and Buffer gas trap are scheduled for delivery during 2007.

At IFA in Aarhus, a "CERN test laboratory" of 100 m^2 has been prepared for tests of the beam line before it is shipped to CERN.

3.4   Cusp trap commissioning in 2007 – 1.5 weeks

During the 2007 beamtime, the following issues will be studied:

1. Ejection and launch of the antiproton blob into the magnetic guiding duct from the MUSASHI trap.

2. Catching the blob by the cusp trap by opening and closing the electric potential gate.

3. Optimizing the transport, trapping, and cooling conditions.

Bibliography

[1] T. Yamazaki *et al.*, Phys. Rep. **366**, 183 (2002).

[2] M. Hori *et al.*, Phys. Rev. Lett. **96**, 243401 (2006).

[3] V.I. Korobov, Phys. Rev. A **67**, 062501 (2003).

[4] V.I. Korobov, Proceedings of EXA05, eds. A. Hirtl, J. Marton, E. Widmann, J. Zmeskal, Austrian Academy of Sciences Press, Vienna 2005.

[5] Y. Kino *et al.*, Hyperfine Interactions **138**, 179 (2001).

[6] P.J. Mohr and B.N.Taylor, Rev. Mod. Phys. **72**, 351 (2000); **77**, 1 (2005).

[7] R.J. Hughes and B.I. Deutch, Phys. Rev. Lett. **69**, 578 (1992).

[8] G. Gabrielse *et al.*, Phys. Rev. Lett. **82**, 3198 (1999).

[9] J. K. Thompson, S. Rainvilleand and D. E. Pritchard, Nature **430** (2004) 58.

[10] R. Holzwarth, Th. Udem, T.W. Hänsch, J.C. Knight, W.J. Wadsworth, and P.St.J. Russell, Phys. Rev. Lett. **85** 2264 (2000).

[11] Th. Udem, R. Holzwarth, and T.W. Hänsch, Nature **416** 233 (2002).

[12] M. Hori *et al.*, Phys. Rev. Lett. **91**, 123401 (2003).

[13] V. Meyer *et al.*, Phys. Rev. Lett. **84**, 1136 (2000).

[14] M. Hori *et al.*, Phys. Rev. Lett. **94**, 063401 (2005).

[15] M. Hori et al Phys. Rev. Lett. 96, 243401 (2006).

[16] E. Widmann et al., Phys. Rev. Lett. 89 (2002) 243402.

[17] D. Bakalov and E. Widmann, submitted to PRA, arXiv:physics/0612021.

[18] A. Kreissl et al., Z. Phys. C 37, 557 (1988).

[19] V. Korobov an D. Bakalov, J. Phys. B 34, L519 (2001).

[20] W.-M. Yao *et al.*, Journal of Physics G **33**, 1 (2006).

[21] G. Ya. Korenman and S.N. Yudin, J. Phys. B 39, 1473 (2006).

[22] H. Yamaguchi *et al.*, Phys. Rev. A **70**, 012501 (2004).

[23] N.Bohr: "On the Constitution of Atoms and Molecules". Philosophical Magazine 26: 1-25 and 476-502 and 857-875 (1913)

[24] N. Bohr: "Penetration of Atomic Particles through Matter" Mat. Fys. Medd. Dan. Vid. Selsk. 18 no 8 (1948)

[25] L.H.Andersen et al "Single and Double Ionization of Helium by Fast Antiproton and Proton Impact" Phys. Rev. Letters 57 2147 (1986) and H. Knudsen and John Reading: "Ionization of Atoms by Particle and Antiparticle Impact" Physics Reports 212 107- 222 (1992)

[26] `http://www.phys.au.dk/amo/collwap/leardata.htm`

[27] See. e.g. S.P.Møller et al "Stopping Power in Insulators and Netals without Charge Exchange" Phys Rev Letters 93 042502-1 (2004)

[28] P. Hvelplund et al: "Ionization of helium and molecular hydrogen by slow antiprotons" J. Phys.B27 925 (1997)

[29] L.H.Andersen et al: "Single ionization of helium by 40-3000 keV antiprotons" Phys Rev A41 6536 (1990)

[30] N. Kuroda, H.A. Torii, K. Yoshiki Franzen, Z. Wang, S. Yoneda, M. Inoue, M. Hori, B. Juhász, D. Horváth, H. Higaki, A. Mohri, J. Eades, K. Komaki, and Y. Yamazaki Phys. Rev. Lett., **94** (2005) 023401.

[31] K. Yoshiki Franzen, N. Kuroda, H. A. Torii, M. Hori, Z. Wang, H. Higaki, S. Yoneda, B. Juhász, D. Horváth, A. Mohri, K. Komaki and Y. Yamazaki, Rev. Sci. Instrum. **74** (2003) 3305.

[32] J. S. Cohen, Rep. Prog. Phys. **67** (2004) 1769; J. S. Cohen, AIP Conf. Proc. **793** (2005) 98.

[33] M. Hori, J. Eades, E. Widmann, T. Yamazaki, R. S. Hayano, T. Ishikawa, H. A. Torii, T. von Egidy, F. J. Hartmann, B. Ketzer, C. Maierl, R. Pohl, M. Kumakura, N. Morita, D. Horváth, I. Sugai. Phys. Rev. A **70** (2004) 012504.

[34] V. L. Varentsov, N. Kuroda, Y. Nagata, H. A. Torii, M. Shibata, Y. Yamazaki. Workshop on Physics with Ultra Slow Antiproton Beams, RIKEN, Wako, Japan (2005). AIP Conf. Proc. **793** (2005) 328.

[35] *Addendum to the proposal CERN/SPSC 97-19 and CERN/SPSC 2000-04*, CERN-SPSC 2005-002/SPSC P-307 Add.1.